Department of Physics and Astronomy
Heidelberg University

Master Thesis in Physics
submitted by

Leo Walz

born in Freiburg (Germany)

2025

Room Temperature Spin Control in High Temperature High Pressure Nanodiamonds

This Master Thesis has been carried out by Leo Walz
at the Physikalisches Institut Heidelberg
under the supervision of

Prof. Dr. Selim Jochim
and
Prof. Dr. Tracy E. Northup
Institut für Experimentalphysik Innsbruck

Abstract

This thesis presents the development and characterization of a new experimental setup specifically designed for studying nanometer-scale diamond particles (nanodiamonds) hosting ensembles of nitrogen-vacancy (NV) color centers. By integrating optically detected magnetic resonance (ODMR) and time-resolved spin readout techniques both, the probing of the NV center's spin and optical properties of individual nanodiamonds are enabled with this system. To complement the experimental advances, a simulation framework is presented to interpret the observed photoluminescence and to elucidate the fundamental processes underlying the NV center's behavior. With these combined capabilities, key physical parameters of the NV system, such as spin relaxation times, spin dephasing rates, and optical emission rates, are quantitatively investigated. Furthermore, ODMR-based sensing capabilities are demonstrated, such as assessing a diamond particles' orientation with respect to an external magnetic field, and quantifying the temperature of the diamond particle via laser-induced heating. Collectively, these results establish a new experimental platform for NV center physics in Innsbruck, paving the way to future research in the direction of levitated, NV center hosting, nanodiamonds.

Diese Arbeit stellt die Entwicklung und Charakterisierung eines neuartigen experimentellen Aufbaus vor, der speziell für die Untersuchung nanometergroßer Diamantpartikel (Nanodiamanten) entwickelt wurde, in denen Ensembles von Nitrogen-Vacancy (NV) centers (Stickstoff-Fehlstellen-Zentren) eingebettet sind. Durch die Kombination von optisch detektierter magnetischer Resonanz (ODMR) und zeitaufgelösten Spin-Auslesetechniken ermöglicht das System die detaillierte Analyse der Spin- und optischen Eigenschaften einzelner Nanodiamanten. Darüber hinaus wird ein Simulationsframework präsentiert, das die beobachtete Photolumineszenz (PL) interpretiert und die grundlegenden Prozesse hinter dem Verhalten der NV-Zentren beleuchtet. Mithilfe dieser kombinierten Ansätze lassen sich zentrale physikalische Parameter des NV-Systems – beispielsweise Spin-Relaxationszeiten, Spin-Defasierungsraten und optische Emissionsraten – quantitativ bestimmen. Ferner werden auf ODMR basierende Sensor-Anwendungen demonstriert, wie etwa die Bestimmung der räumlichen Orientierung der Diamantpartikel relativ zu einem externen Magnetfeld und die Quantifizierung ihrer Temperatur durch laserinduzierte Erwärmung. Insgesamt etabliert diese Arbeit eine neue experimentelle Plattform für die Erforschung von NV-Zentren in Innsbruck und ebnet den Weg für zukünftige Untersuchungen an levitierten, NV-Zentren beherbergenden Diamantpartikeln im Nanometerbereich.

Contents

1. Introduction **3**
- 1.1. Motivation . . . 3
- 1.2. Thesis Outline . . . 5

2. The Nitrogen-Vacancy Color Center **6**
- 2.1. Intrinsic Properties of the Nitrogen-Vacancy Center at Room Temperature 6
- 2.2. Effects of the Diamond Lattice . . . 7
  - 2.2.1. Orientation of the Nitrogen-Vacancy Center inside the Diamond Lattice . . . 8
  - 2.2.2. Thermal Shift of the 3A2 Zero Field Splitting . . . 10
  - 2.2.3. Effects of Diamond Size on Photon Emission . . . 11
- 2.3. Simulation of the Nitrogen-Vacancy Center . . . 12
  - 2.3.1. The Simulation Model . . . 14
  - 2.3.2. Simulation Parameters . . . 16
  - 2.3.3. Numerical Solutions to the Master Equation . . . 17
  - 2.3.4. Understanding the Nitrogen-Vacancy Center's Spin Initialization and Readout Process . . . 19

3. Experiment Setup and Methods **21**
- 3.1. Experimental Setup . . . 21
  - 3.1.1. Confocal Microscope . . . 21
  - 3.1.2. Preparation of Nanodiamond Particles . . . 23
  - 3.1.3. Photon Detection . . . 24
  - 3.1.4. Resonant Microwave Driving . . . 26
  - 3.1.5. Experiment Control with ARTIQ . . . 26
- 3.2. Experimental Techniques . . . 27
  - 3.2.1. Pulsed Spin Readout . . . 27
  - 3.2.2. Optically Detected Magnetic Resonance Spectroscopy . . . 30

4. Results and Measurements **31**
- 4.1. Fluorescence Spectrum . . . 31
- 4.2. Radiative Decay Rate . . . 32
- 4.3. Optical Saturation . . . 36
  - 4.3.1. Simulating the Optical Saturation of the Nitrogen-Vacancy Center 36
  - 4.3.2. Measured Optical Saturation . . . 39
- 4.4. Lifetime of the Singlet States Manifold . . . 40
- 4.5. Ground State Spin Relaxation Time . . . 43

4.6. Optically Detected Magnetic Resonance Spectroscopy Measurements . . . 45
4.6.1. Measuring Temperature and Laser Induced Heating 45
4.6.2. Determining the Diamond Particle's Orientation with respect to an External Magnetic Field 47
4.6.3. Optically Detected Magnetic Resonance Spectroscopy with Nanodiamonds 49
4.7. Electronic Spin Coherence of the Nitrogen-Vacancy Center 51

5. Discussion and Outlook **53**
5.1. Experimental Setup 53
5.2. NV center Properties in Diamond Particles 54

A. Appendix **56**
A.1. Saturation Intensity 56
A.2. Orientation of the DC Magnetic Field with respect to the Diamond Crystal Orientation 58

1. Introduction

1.1. Motivation

The maximum speed at which any information can travel, according to special relativity, is limited by the speed of light in vacuum. From this limited speed of information transfer we infer that for any two separate events to have a direct relationship of cause and effect, the information of the cause-event must have had the chance to reach the effect-event in time.

At the same time, quantum mechanics predicts that the observation outcome of any system is fundamentally probabilistic. For example, a binary quantum system can be prepared in a state where the probabilities of measuring either outcome (0 or 1) are equal for a particular choice of basis. In essence this is analogous to a coin-toss machine but one where the randomness of the outcome is guaranteed by quantum mechanics. Such a machine is often called a Quantum Random Number Generator (QRNG).

Now from this we might expect the measurement outcomes of two QRNGs separated by a great distance to be fully independent. More precisely, if two such QRNGs that are well separated from each other were measured at exactly the same time, ensuring that no information about the measurement basis or outcome of one QRNG could reach the other fast enough, then these two outcomes should be statistically independent. In this example, statistical independence means that the outcomes will be the same in half the cases and different in the other half.

In 2015 an experiment was performed by Hensen et al. [1] in which two such QRNGs[1] were placed 1.3 km apart and their state measured at the same time. Moreover, the measurement time for each QRNG was significantly shorter than the minimum time required for any information to travel between the QRNGs and potentially influence the outcome. In this, Hensen et al. found that the measurement outcomes of these two QRNGs were correlated to a much greater degree than explainable with statistical independence. Currently, quantum mechanics is the only established theory explaining such measurement statistics where they are the consequence of a property called entanglement.

Note that such an outcome does not imply a violation of special relativity specifically. This is due to the fact that each individual measurement outcome is still random and the correlations are only apparent after the measurement outcomes have been shared via a classical communication channel (for example fiber optics), thus, no information was

[1] To avoid confusion: In the paper by Hensen et al. they refer to QRNGs as separate devices that are used as a source of randomness to determine a random measurement basis for the entangled NV centers. In this chapter such random basis selection by a separate quantum device is included into the measurement action of the QRNG as defined above.

actually transmitted. Such outcomes mean that any theory adhering to the informational speed limit and quantum mechanics must violate the concept of local realism to explain these correlations [2].

These findings by Hensen et al. were generally expected. Similar experimental results were been observed many years prior, such as the experiments [3–5], for which experimentalists were awarded the 2022 Nobel prize in Physics. The significance of the work done by Hensen et al. lies in it being the first experiment to simultaneously close the two remaining possible loopholes, which in previous experiments came up as further assumptions had to be made about imperfect experimental setups [1]. This experimental breakthrough of Hensen et al. made use of a relatively new quantum system: a solid state spin qubit based on a single nitrogen-vacancy (NV) color center in diamond.

Most of the NV center's quantum properties have only been investigated since the turn of the millennium [6]. However, its long electron spin coherence time, combined with the possibility of fast and high-fidelity state preparation as well as single-shot readout [7], quickly enabled the NV center's success in quantum information experiments.

Other useful features of NV centers are their strong spin localization and spin lifetime at room temperature, coupled with the capability of optical readout. This has facilitated applications for probing materials' temperature, strain, and electric or magnetic fields at the nanometer scale [8].

Lastly, one further interesting feature of the NV center is that the magnetic moment associated with the NV center's spin is, through its strong localization in the diamond lattice, coupled to the entire diamond particle. One could, for instance, imagine an experiment analogous to a Stern-Gerlach type interferometer [9], where the motion of a sufficiently isolated diamond particle becomes entangled with the internal NV spin qubit, effectively creating a spatial superposition of the particle itself. Although technically challenging, such an experiment might pave the way to realizing Feynman's proposal, presented at the Chapel Hill conference, of entangling a test mass with a spatial superposition of a source mass solely via their gravitational interaction [10].

Similarly, as two entangled NV centers crowned decades of experimental effort to decisively reject a broad class of local realistic hidden variable models as underlying descriptions of quantum phenomena, solid-state spin qubits entangled with their host masses could provide insights into the classical or quantum nature of the gravitational field itself. While conducting such a tabletop experiment currently appears technically daunting, research into macroscopic quantum systems has only recently begun [11].

1.2. Thesis Outline

While being motivated by the above, in this thesis I not attempt to realize the far-reaching goals but instead focus on laying the groundwork within our research group by developing initial experimental tools and methods for tabletop experiments with levitated nanoscale diamond particles. The research was carried out in the group of Tracy E. Northup at the university of Innsbruck and also closely supervised by Simon Baier. This thesis is focused on the study and control of NV centers in room-temperature diamond particles. To achieve this, the thesis is structured as follows: In Chapter 2 I present a theoretical framework of NV centers at room temperature inside nanodiamonds. Chapter 3 focuses on the experimental apparatus. Section 3.1 presents the design and experimental implementation, while Section 3.2 outlines the experimental techniques successfully integrated into the setup. This setup facilitated the measurement of NV center properties, and also demonstrates various sensing capabilities, in diamond particles, with the results detailed in Chapter 4. Chapter 5 concludes the thesis with a discussion of the main achievements and an outlook on further measurements.

2. The Nitrogen-Vacancy Color Center

This chapter provides a short overview about the most relevant properties of the NV center, given the work described in this thesis. Here only the properties of the negatively charged NV center at room temperature are discussed, leaving out the NV center's behaviour in a cryogenic environment, or in a neutral charge state. In addition, I selectively highlight the influence of the diamond crystal on the NV center. Finally, a simulation framework for the dynamics of the NV center is presented. For a thorough review on NV center properties, the reader is referred to the review by Doherty et al. [6].

2.1. Intrinsic Properties of the Nitrogen-Vacancy Center at Room Temperature

The NV center is a substitutional point defect in diamond. It consists of a nitrogen atom substituted for a carbon atom and paired with an adjacent lattice vacancy. The NV center exhibits tetrahedral C_{3v} symmetry, where the axis of the nitrogen-vacancy pair is parallel to the diamond's crystallographic $\langle 1,1,1\rangle$ directions (see further in figure 2.2). The NV center naturally occurs in its neutral $\mathtt{NV}^0$ state or can also accept an electron might donated by another isolated nitrogen defect [12], forming the more stable, negatively charged $\mathtt{NV}^-$ state, which will be the focus of this work. Unless stated otherwise, "NV center" will refer to the $\mathtt{NV}^-$ state throughout this thesis.

Figure 2.1 shows the widely accepted $\mathtt{NV}^-$ level scheme, which at room temperature consists of four accessible electronic states that are situated deep within the diamond band gap (approx. 5.4 eV [13]): These include the 3A2 ground and 3E excited spin-triplets, along with two intermediary spin-singlet states: 1E and 1A1 . The 3E actually consists of two orbitals, $\mathtt{3E}_x$ and $\mathtt{3E}_y$, which are both spin-triplets. However, these two orbitals are only spectrally resolvable at cryogenic temperatures, and at higher temperatures, phonon mediated hopping between them dominates, averaging them into a single spin-triplet state 3E [14, 15]. Due to spin-spin interaction, the $m_s = 0$ and $m_s = \pm 1$ spin projections of the 3A2 and 3E triplet states are split by the zero-field splittings (ZFS), D, of approximately 2.87 GHz and 1.42 GHz, respectively [6], however, in this work any further reference to ZFS will refer to the ZFS of the 3A2 state. The 3A2 state has an electron g-factor of 2.0028 [6], which will be approximated as two throughout this thesis.

Crucial to the NV center's dynamics are the intersystem crossings (ISC) 3E $\rightarrow$1A1 and

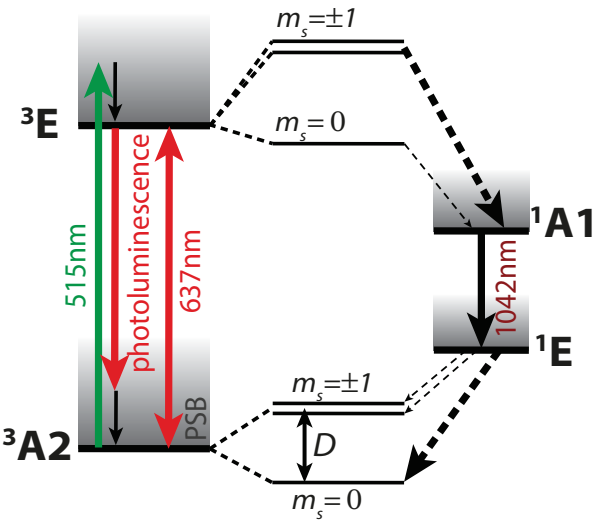

Figure 2.1.: **Fine Structure of the NV$^-$ at Room Temperature**
Optical transitions are drawn as solid arrows, with the zero-phonon line (ZPL) at 637 nm (1.945 eV) and 1042 nm (1.19 eV). Shaded areas represent phonon sidebands, which result from the coupling of the electronic states with lattice vibrations. Phonon transitions between the electronic triplet and the electronic singlet states are drawn as dashed arrows with the thickness indicating a relative transition probability. We drive the 3A2 →3E transition by a 515 nm laser and measure photoluminescence (PL) above 561 nm.
Transitions between the $m_s = 0$ and $m_s = \pm 1$ spin projections of the 3A2 ground state can be driven by a resonant microwave (mw) magnetic field. Note, while the 3E also has a ZFS, D, this is not drawn here.

1E →3A2 . In figure 2.1 these are drawn as dashed black arrows, where the thickness indicates a relative transition probability. These phonon transitions making up the ISC are spin-selective, this enables state preparation via optical pumping as well as the spin readout schemes described in this thesis.

2.2. Effects of the Diamond Lattice

NV centers are a remarkable quantum platform, showing a spin coherence of the 3A2 ground states in the millisecond range even in room temperature diamonds under atmosphere [16]. This is facilitated by the fact that the NV center states are situated deep inside the diamond band gap. Being confined inside a crystal, however, does have some noticeable consequences on the quantum system. In this section, these effects of the diamond lattice, which are observed in the measurements detailed in chapter 4, are described further.

2.2.1. Orientation of the Nitrogen-Vacancy Center inside the Diamond Lattice

Diamond refers to a specific solid state of pure carbon where each carbon atom is bonded to four other carbon atoms by four sp3 covalent bonds in a tetrahedral structure. This isotropic tetrahedral structure results in a highly symmetric crystal also known as a face centered cubic crystal, denoted Fd3m. Introducing an NV defect into this crystal reduces this high symmetry to the C_{3v} point group. In figure 2.2 the structure of the NV center within the diamond lattice is reproduced from [17]. As can be seen there, the axis of the NV center is parallel to the axis of the carbon-carbon bond that it replaces. Inside the diamond crystal, this axis is denoted by the crystallographic $\langle 1, 1, 1 \rangle$ direction. The tetrahedral structure of the diamond crystal lends four possible distinct $\langle 1, 1, 1 \rangle$ orientations in which each individual NV center can be oriented (figure 2.2). In the manufacturing of NV-center-doped diamonds, most techniques, including the one that produced our diamonds, rely on the stochastic process of mobile vacancy and nitrogen defects to 'find' each other and form the lower-energy NV center state. This is often done in a high temperature annealing step. This process leaves randomly oriented NV centers with respect to these four orientation possibilities. At room temperature the mobility of the individual defects is negligible and the NV centers remain stable.

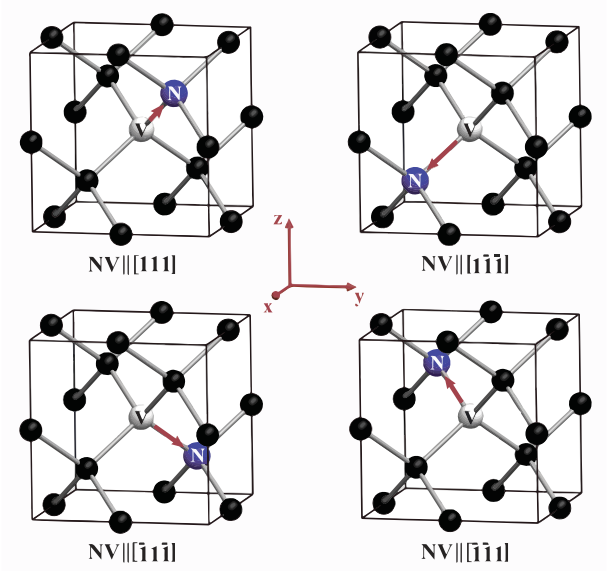

Figure 2.2.: **Orientation of the Nitrogen-Vacancy Center Inside the Diamond** Inside a mono-crystalline diamond lattice, four possible orientations of the NV center exist. Carbon atoms are depicted in black, nitrogen in blue and the vacancy in white. The four figures show possible $\langle 1, 1, 1 \rangle$ directions for the NV center to be oriented in. In each figure, the axis of the $\mathtt{NV}^-$ spin is drawn as a red arrow, and each NV center orientation is labeled with its parallel crystallographic axis [hkl] indexing the direction in the basis of the direct lattice vector spanned by the coordinate system shown in the center (red). The illustration is recreated from [17].

Working with diamond samples containing ensembles of NV centers, one has to consider the fact that the spin transitions associated with these four orientations of the NV axis are degenerate. This degeneracy is lifted by a magnetic field. Because of the Zeeman effect, the magnetic field causes an energy shift, δE_i, in the spin states of each NV center orientation i. This energy shift is given by

$$\delta E_i = \frac{\mu_B g \cdot \vec{S}_i}{\hbar} \cdot \vec{B}. \tag{2.1}$$

Here μ_B is the Bohr magneton, $\hbar$ the reduced Planck constant, g the electron g-factor (as stated above, for the 3A2 state $g \approx 2$) and $\vec{S}_i$ the spin vector of the NV center at site i. We can rewrite equation (2.1) in the basis of the four possible lattice orientations $\hat{n}_i \in \{\hat{n_1}, \hat{n_2}, \hat{n_3}, \hat{n_4}\}$ as

$$\delta E_i = \mu_B g m_{s,i} \vec{B} \cdot \hat{n}_i \tag{2.2}$$

where $\hbar m_{s,i} = S_{z,i}$ now refers to the quantization value of the NV center's spin ($m_{s,i} \in \{0, 1, -1\}$) with respect to the quantization axis, set by the site i whose direction is given by the unit vector $\hat{n}_i$. The observation of this Zeeman shift for different NV center orientations will be described in section 4.6.2. There the frequency splitting $\Delta\omega = \frac{1}{\hbar}(E_{m_s=+1} - E_{m_s=-1})$ between the two $|m_s| = 1$ states is used, which is defined as

$$\Delta\omega_i = \frac{2\mu_B g}{\hbar} \vec{B} \cdot \hat{n}_i. \tag{2.3}$$

2.2.2. Thermal Shift of the 3A2 Zero Field Splitting

The NV center can act as a temperature sensor. This comes from the thermal dependence of the ZFS (figure 2.1). This ground state ZFS results from the electron spin-spin interaction, which is dependent on the spatial distance between spins. For the 3A2 ground state, simulations have shown that these spins are localized around the NV center in an effective spin density that mostly originates from the dangling sp3 bonds of the three carbon atoms surrounding the vacancy site [13, 18]. In a recent work by Tang et al. [19], it was shown that the temperature dependence of the ZFS can be accounted for by considering the temperature-induced displacement of the carbon atoms close to the NV center. This led Cambria et al. [20] to derive an analytical model in which the temperature dependence is described as a series expansion of different phonon mode contributions. In the following, their model for the ZFS temperature dependence will be summarized. The temperature dependence of the ZFS, $D(T)$, is described by the expansion

$$D(T) = D_0 + \sum_{i=1}^{M} c_i n_i \tag{2.4}$$

where M is the number of representative phonon modes; c_i their coefficients, which also include the effects of other modes with similar energies; and n_i the mean occupation number of the i-th mode, given by the Bose-Einstein distribution

$$n_i = \frac{1}{e^{\Delta_i / k_B T} - 1},$$

where Δ_i is the mode energy and k_B the Boltzmann constant. Cambria et al. find that restricting equation (2.4) to $M = 2$ is sufficient to capture the behaviour of the ZFS as a function of temperature, leading to the expression

$$D(T) = D_0 + c_1 n_1 + c_2 n_2. \tag{2.5}$$

The parameters D_0, c_1, Δ_1, c_2 and Δ_2 are experimentally obtained as free fit parameters (table 2.1).

Parameter	**Value** [meV]	**Parameter**	**Value** [MHz]
		D_0	2877.38 ± 0.03
Δ_1	58.73 ± 2.32	c_1	-54.91 ± 7.35
Δ_2	145.5 ± 8.4	c_2	-249.6 ± 19.4

Table 2.1.: Parameter values for Equation (2.5) taken from [20]

2.2.3. Effects of Diamond Size on Photon Emission

In most of the literature, the intrinsic NV properties such as optical (radiative) decay rates are measured in bulk diamond samples [14, 21–23]. However, nanodiamond-hosted NV centers can experience a suppression of these radiative rates if the host diamond is of a size comparable to or smaller than the optical wavelength. Generally the rate of spontaneous decay of an emitter surrounded by a dielectric medium of refractive index n will have a significant influence over its optical properties.

Let us first consider the limiting case of an emitter surrounded only by a vacuum and compare that to the case of an emitter situated inside a large (compared to the emission wavelength) dielectric medium of refractive index n. Inside the dielectric medium, the electric field amplitude is $1/n$ smaller. Also, the photon mode density, which refers to the number of photon modes of a frequency between ω and $\omega + \mathrm{d}\omega$ per unit volume, is greater by a factor of n^3 inside the dielectric medium. We can quantify these influences by using Fermi's golden rule [24] to calculate the rate of spontaneous decay, $\Gamma_{e\to f}$, from an excited state $|e\rangle$ to a final state $|f\rangle$. This is given as

$$\Gamma_{e\to f} = \frac{2\pi}{\hbar^2} |M_{fe}|^2 \, g(\omega_f). \tag{2.6}$$

where M_{ij} are the transition matrix elements and $g(\omega_f)$ is the density of final states, and using the fact that $M_{ij}^{[\mathrm{bulk}]} \sim n M_{ij}^{[\mathrm{vac}]}$, we obtain a linear dependence of the spontaneous emission rate Γ when the emitter is placed inside a bulk dielectric medium ($\Gamma_{[\mathrm{bulk}]}$) compared to when it is placed inside vacuum ($\Gamma_{[\mathrm{vac}]}$),

$$\Gamma_{[\mathrm{bulk}]} \sim n \Gamma_{[\mathrm{vac}]}. \tag{2.7}$$

This treatment, however, does not consider the boundary conditions created by a small (compared to the emission wavelength) dielectric medium when using nanodiamonds.

A more refined description includes local-field corrections based on the shape of the nanodiamond. When a nanodiamond becomes smaller than the optical wavelength of emitted light, inside the diamond, no internal field modes are supported. Then, the rate of spontaneous decay via photon emission of an NV center, $\Gamma_{[\mathrm{nd}]}$, compared to the rate of spontaneous decay of an NV center inside a bulk diamond, $\Gamma_{[\mathrm{bulk}]}$, can be approximated by

$$\Gamma_{[\mathrm{nd}]} = \frac{\eta^2}{n}\Gamma_{[\mathrm{bulk}]} \tag{2.8}$$

where n is the refractive index of diamond and η is a local-field correction factor [25]. For a spherical particle the local-field correction factor in equation (2.8) is given by

$$\eta_{\mathrm{sphere}} = \left(\frac{3}{2+n^2}\right) \tag{2.9}$$

and does not depend on the orientation of the NV center's dipole moment inside the nanodiamond. In the case of an ellipsoidal nanodiamond, the local-field correction is angle-dependent, and one has to use the ensemble average $\langle\eta^2\rangle$ for three directions of transition dipole moment orientations with respect to the three ellipsoidal axes. The results can then vary greatly depending on the actual shape of the nanodiamond. As this shape is often not known, Plakhotnik and Aman [25] calculate an average expected suppression by restricting the shape of nanodiamonds to ellipsoids where the shortest ellipsoid axis is maximally 1/2 the length of the longest. Doing so, they find a mean ($\pm$ 1 standard deviation) expected rate of spontaneous decay of NV centers inside nanodiamonds that are surrounded by air of

$$\Gamma^{\mathrm{avg}}_{[\mathrm{nd}]} \approx 0.07(3)\Gamma_{[\mathrm{bulk}]}. \tag{2.10}$$

Lastly, we need to consider that in the experimental setup used in this thesis, the investigated nanodiamonds are sandwiched between two glass slides (section 3.1). These external glass slides enhance the optical emission rate [26]. To consider this effect, we will use the estimate of an enhancement of emission rate by 1.7 [25]. This value is doubled to account for the two glass slides, which yields an estimate for the expected observable decay rate ($\Gamma^{\mathrm{obs}}_{[\mathrm{nd}]}$) of

$$\Gamma^{\mathrm{obs}}_{[\mathrm{nd}]} \approx 2 \times 1.7 \times 0.07\Gamma_{[\mathrm{bulk}]} = 0.24\Gamma_{[\mathrm{bulk}]}. \tag{2.11}$$

This corresponds to an expected suppression of optical emission by a factor of 4.2.

2.3. Simulation of the Nitrogen-Vacancy Center

In the following a simulation model is introduced which aims to support the experimental observations and detail the underlying dynamical behaviour of the NV center. The simulations will be used in chapters 3 and 4 to gain a deeper understanding of the underlying physical processes in the observed data.

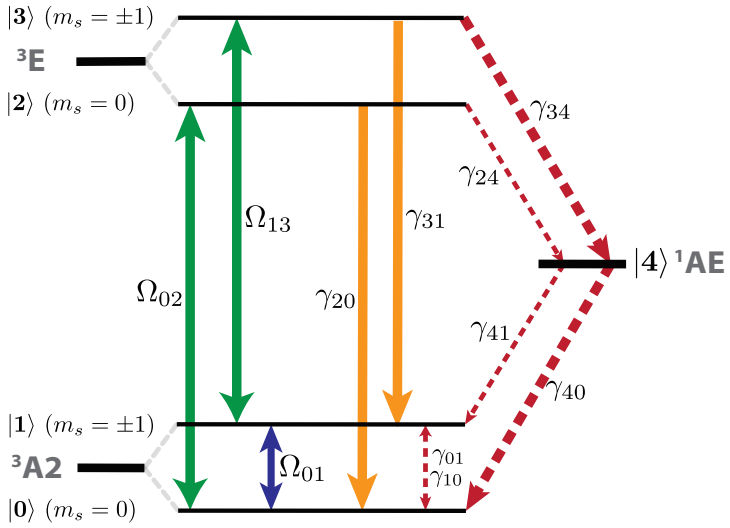

Figure 2.3.: **Reduced Level Scheme for Simulations of the NV$^-$ Center**
A reduced level scheme of the NV$^-$ as it is used for simulations within this thesis is depicted. The individual states are labeled from $|0\rangle$ to $|4\rangle$. The rabi couplings (solid green arrow) are denoted as Ω_{ij} but are symmetric ($\Omega_{ij} = \Omega_{ji}$). Note: The laser driving the optical coupling is in reality off-resonant involving stokes absorption - but is modeled as resonant here. Radiative decay channels are drawn as a solid orange and non-radiative channels in dashed red lines. γ_{ij} denotes the rate of decay $|i\rangle \rightarrow |j\rangle$.
Compared to figure 2.1 only one effective singlet state '1AE' is used, subsuming the true 1A1 and 1E states. Further, the $m_s = +1$ and $m_s = -1$ spin projections of the 3A2 and 3E states are combined into one $m_s = \pm 1$ state each, where the populations of these combined states corresponds to the sum of the populations in the $m_s = -1$ and $m_s = 1$ states.

2.3.1. The Simulation Model

Describing the NV center's dynamical PL requires solving the time evolution of a system with at least five states. The following model based on a Lindblad Master Equation, is adapted from [27] and captures the essential dynamics of the NV center states that are accessible in the performed experiments. A more physically motivated Hamiltonian is discussed in [28] and [29].

For the simulation, we first construct the Hamiltonian of the closed quantum system. This Hamiltonian is described as a sum of a time-independent part, H_0, and a time-dependent perturbation, H_1, such that

$$H = H_0 + H_1. \tag{2.12}$$

The time dependence of H will later be dropped by transforming it into the rotating frame. H_0 can generally be written in diagonal form as

$$H_0 = \sum_{i=0}^{N-1} E_i \left|i\right\rangle \left\langle i\right| \tag{2.13}$$

where E_i (the energy of state i) are the eigenvalues of the eigenvectors $|i\rangle$ of H_0. Here, it is convenient to set the lowest energy of the system to zero ($E_0 = 0$) such that all other energies are relative to E_0. In using this approach to construct H_0 we do not require any further information about the eigenstates $|i\rangle$ and just use them as an orthonormal basis in which we describe the dynamics of the perturbed system. This perturbation is introduced in the form of resonant pairwise coupling between two states $|i\rangle$ and $|j\rangle$ by the Hamiltonian

$$H_1 = -f(t)\frac{\hbar\Omega_{ij}}{2}(\sigma_{ij} + \sigma_{ji}) \tag{2.14}$$

where Ω_{ij} is the real valued rabi frequency and σ_{ij} are the state operators defined as

$$\sigma_{ij} = \left|i\right\rangle \left\langle j\right|.$$

The function $f(t)$ is later passed into the solver separately and is used to modulate the strength of this coupling Ω_{ij} (e.g. to implement a 'real' laser pulse). The coupling described in equation (2.14) could for example be obtained as the result of a resonant driving oscillating field interacting with $|i\rangle$ and $|j\rangle$ via a dipole moment. The resonance condition means that the driving frequency ω_{ij}^{d} has a zero detuning Δ_{ij} to the frequency difference between the two states $|i\rangle, |j\rangle$ such that

$$\Delta_{ij} = \frac{1}{\hbar}(E_j - E_i) - \omega_{ij}^{\mathrm{d}} = 0 \qquad\qquad (E_i \leq E_j) \tag{2.15}$$

In such a case, H_1 is obtained by a unitary transformation into the rotating frame of the driving frequency

$$H_1 = U^{\dagger} H_1' U \tag{2.16}$$

where H_1' is the interaction Hamiltonian capturing the dipolar interaction of the states $|i\rangle, |j\rangle$ with the field after the so called rotating wave approximation is used to cancel fast

(compared to the driving frequency ω_{ij}^{d}) rotating terms. This unitary in equation (2.16) is defined as

$$U = e^{-i\omega_{ij}^{\mathrm{d}}\sigma_{jj}t} \tag{2.17}$$

and $U^\dagger$ is the hermitian conjugate of U. For the simulations used in this thesis we will only consider resonant driving ($\Delta_{ij} = 0$).

In the simulated NV center system (see figure 2.3) the `1AE` state is not coupled to with any coherent (i.e. rabi, Ω_{ij}) couplings but only via dissipative (decay) processes. These decay processes are described via jump operators, which will be introduced next. One consequences of describing this process via jump operators only is that we can set the energy of this state to zero without any changes in the resulting physics. The result of this is a Hamiltonian for the closed system that has a diagonal of zeros and only includes off-diagonal elements corresponding to a resonant driving between certain states such that the total Hamiltonian used for calculations becomes

$$H = -\sum_{j>i} f_{ij}(t)\frac{\hbar\Omega_{ij}}{2}(\sigma_{ij} + \sigma_{ji}). \tag{2.18}$$

We now turn to the dissipative parts of this system. To simulate the dynamics of the open quantum system, we use the Lindblad master equation in the form of

$$\frac{d\rho}{dt} = -\frac{i}{\hbar}[H, \rho] + \sum_k \left(L_k \rho L_k^\dagger - \frac{1}{2}\{L_k^\dagger L_k, \rho\} \right) \tag{2.19}$$

where ρ is the density matrix, defined as

$$\rho = \sum_{i,j} \rho_{ij}\sigma_{ij}. \tag{2.20}$$

Here L_k are collapse operators, used to introduce the dissipative parts of the system's dynamics. Spontaneous decay from the state $|i\rangle$ to $|j\rangle$ is given by the collapse operator

$$L_{ji} = \sqrt{\gamma_{ij}}\sigma_{ji}$$

where γ_{ij} denotes the spontaneous decay rate from state $|i\rangle$ to state $|j\rangle$[1]. From equation (2.19) it follows, that under dissipative dynamics only, the rate at which an initial state $|i\rangle$ decays is given by the sum of all decay channels, and thus the lifetime, often denoted as T1, of a state $|i\rangle$ can be written as

$$\mathrm{T1}_{|i\rangle} = \frac{1}{\sum_j \gamma_{ij}}. \tag{2.21}$$

In many quantum systems, the coherence of a quantum state is not limited by decay but rather by dephasing. This thesis does not aim to investigate dephasing mechanisms

[1]Note this definition of L_k switches the order of indices i and j for the decay rate γ_{ij} compared to commonly used notation. This is done here to make the indexation of the decay rates used later in this thesis more intuitive.

of the NV center but includes an effective dephasing operator in the Lindblad master equation written as:

$$L_i = \sqrt{\gamma_{ii}}\sigma_{ii} \tag{2.22}$$

where γ_{ii} gives the rate of dephasing of the state $|i\rangle$, empirically providing an exponential decay rate for the coherence of the state. For a single channel, this decoherence rate relates to the often used coherence time, T2 via

$$\mathrm{T2}_{|i\rangle} = \frac{1}{\gamma_{ii}}. \tag{2.23}$$

2.3.2. Simulation Parameters

In this thesis many dynamical effects of NV color center hosting diamond particles are measured. The simulation framework introduced in section 2.3 is overlayed with these measurements in order to give a more complete picture on the underlying dynamics of the NV center system. In order to do this, the set of parameters of table 2.2 are used. Here, where possible, values are directly extracted from measurements in chapter 4. γ_{01}, γ_{10} and γ_{11} are results of direct measurement described in section 4.5 and section 4.7. The parameters $\gamma_{20}, \gamma_{31}, \gamma_{34}, \gamma_{24}$ describe the decay processes of the excited 3E manifold. Individually resolving these is not possible with the current setup thus the values γ_{34} and γ_{24} are taken from literature, and the values of γ_{20}, γ_{31} are deduced by a combination of experiment as well as consulting the literature values γ_{34}, γ_{24}. This is further described in section 4.2. Similarly, the values γ_{40} and γ_{41} are a combination of measurement and the branching ratio reported in literature, see section 4.4. Lastly, the fast dephasing rate of the 3E states is added as a qualitative value for the fast photon-phonon coupling that is introduced to remove coherent oscillations that would otherwise be observed in the simulations. This is motivated by the fast relaxation of vibrationally excited states which are on the picosecond timescale [25]. By comparing different simulations, an increase of this rate beyond 10 GHz does not qualitatively change the simulation outcome if the driving power is rescaled accordingly (see section 4.3.1).

Parameter	Value [MHz]	Description
γ_{20}, γ_{31}	19.5 ± 1.7	`3E` optical emission rate Section 4.2
γ_{34}	75 ± 16	ISC: `3E` ($m_s = \pm 1$) $\rightarrow$ `1AE` Section 4.2
γ_{24}	9.8 ± 1.4	ISC: `3E` ($m_s = 0$) $\rightarrow$ `1AE` Section 4.2
γ_{40}	22	ISC: `1AE` $\rightarrow$ `3A2` $m_s = 0$ Section 4.4
γ_{41}	11	ISC: `1AE` $\rightarrow$ `3A2` $m_s = \pm 1$ Section 4.4
γ_{01}, γ_{10}	3.6×10^{-3}	`3A2` spin relaxation rate Section 4.5
γ_{11}	0.26(6)	`3A2` spin decoherence rate Section 4.7
γ_{22}, γ_{33}	10^5	Empirically added dephasing rate

Table 2.2.: **Decay Rates as used in the Nanodiamond Simulations:** If not explicitly stated otherwise the following decay rates are used as simulations parameters for Nanodiamond simulations. The decay rates here refer to the level scheme drawn in figure 2.3. We emphasize that the values obtained for γ_{40} and γ_{41} in section 4.4 differ from other literature values and are not fully understood.

2.3.3. Numerical Solutions to the Master Equation

In the previous sections a master equation approach was formulated, which, given the correct parameters, lends the capability to describe the time evolution of the described NV system. Apart from section A.1 all solutions of the master equation equation (2.19) have been obtained numerically. This was achieved by implementing the functionality of the Quantum Toolbox in Python (QuTiP) package [30]. In the following a quick overview of the core functions from the QuTiP package are presented.

First in Source Code 1 for solving the time evolution of the system QuTiP's master equation solver `mesolve` is used. the results of these computations are shown in sections 2.3, 3.2.1, 4.2 and 4.4.

Another possibility is to directly compute the steady state of the system via the function `steadystate()`, see Source Code 2. This computation of the steady state solution is used in section 4.3.1.

Note that the source code examples shown in Source Codes 1 and 2 are only cutouts to the core parts. The complete source code to this simulator is planned to become publicly available here [33].

```python
import qutip as qt
opts = {
    "store_final_state": True,
    "store_states": True,
    "progress_bar": "enhanced" if progress_bar else None,
    "nsteps": nsteps,
}
result = qt.mesolve(
    H=self.H_total,
    rho0=rho_0,
    tlist=time_points,
    c_ops=self.L,
    e_ops=[v * v.dag() for v in self.basis],
    options=opts,
    )
```

Source Code 1: **Numerically Compute the Time Evolution of the System**
Here a cutout of the most relevant source code is shown where the time evolution of the system defined by equation (2.19) is computed for a given initial state ρ_0 via the function `mesolve()` [31].

```python
import qutip as qt

result = qt.steadystate(
    A=H_total,
    c_ops=self.L,
    )
```

Source Code 2: **Numerically Compute the Steady State of the System**
A cutout of how the steady state of the system is computed using the function `steadystate()` [32]. Note that this requires a single time independent Hamiltonian (i.e. the modulation function $f(t)$ in equation (2.18) needs to be dropped.)

2.3.4. Understanding the Nitrogen-Vacancy Center's Spin Initialization and Readout Process

Lastly, in this chapter I present an example simulation which aims to show the internal NV dynamics and explain how they are utilized for the spin manipulation and readout techniques used within this thesis.

When it comes to NV center research, most initialization and readout techniques are based on optical coupling to the NV center. Here illumination with blue detuned (green laser) light can offer both, initialization and readout. Such green light illumination is a popular choice in many experiments, as it can be implemented with almost no constraints on the light used (even using green LED's is possible [34]). It should be noted though that readout techniques using green light illumination fail to provide single shot readout of individual NV centers, as for this resonant illumination and/or spin to charge conversion techniques are necessary. For an overview of different readout mechanisms the reader is referred to [7].

In this thesis off-resonant excitation via a green laser is used for initialization as well as readout. Such optical initialization and readout is facilitated by the fact that diamond has a band gap of approximately 5.4 eV which renders the pure diamond host crystal transparent to the relevant wavelengths. A useful optical property of the NV center in this context is its strong coupling of phonons to the bare optical transmission, the zero phonon line (ZPL), see also section 4.1. This strong coupling mainly helps in two aspects. Firstly it enables the previously mentioned off-resonant (compared to the actual ZPL) driving with green laser light. Secondly, as most of the fluorescence exhibits a large Stokes shift toward longer wavelengths, this light can now be spectrally separated from elastically scattered laser light using optical filters.

Let us now turn to the initialization and readout process, via optical coupling. These rely on the interplay of spin selective intersystem crossings and pumping into the singlet state manifold subsumed in `1AE` . An example simulation of this process is given in figure 2.4. It shows the dynamical change of state populations under the excitation of a 1 µs long realistic laser pulse, coupling `3A2` to `3E` , at an intensity of I_{sat}. The initial state of the simulation is a spin mixture of the three spin projections of the `3A2` spin triplet state. Note here, that in all simulations throughout this thesis, due to their identical dynamics, we sum the populations of the $m_s = 1$ and $m_s = +1$ projections in both spin triplet states (`3A2` and `3E`) and only show the combined populations denoted as $\sum m_s = \pm 1$.

In this simulation two main effects can be observed. First when considering the PL (solid orange line) it is apparent that the initial PL starts low, raises under optical excitation and eventually reaches a steady state. The initial lower PL is a result of the $m_s = \pm 1$ manifold having a greater probability of becoming temporarily shelved in the "dark" `1AE` state. Depending on the driving power, an equilibrium PL is reached after a short time period, in this case after about 500 ns. The difference in PL depending on the spin state will also serve as the basis of the spin readout mechanism presented in section 3.2.1.

Secondly a focus is given on the populations of the two different spin projections of

the 3A2 ground state. In figure 2.4 these are drawn in dashed-blue for the $m_s = \pm 1$ and solid-blue for the $m_s = 0$ manifold of 3A2 . Here, it is notable how the population of the $m_s = \pm 1$ projection quickly drops while the population of the $m_s = 0$ projection rises. The reason behind this spin pumping is, that the $m_s = \pm 1$ states have a greater chance of undergoing an ISC into the singlet state manifold, and then also are more likely to decay into the $m_s = 0$ ground state from the 1AE manifold. This means that after only a few optical cycles the spin state becomes polarized, which remains after the laser driving has been switched off, only decaying at a timescale of T1. In the simulation of figure 2.4 a final polarization of 0.84 is reached.

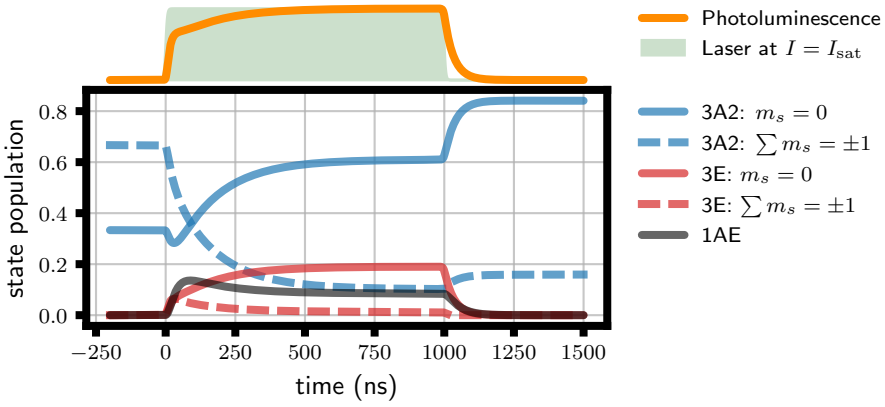

Figure 2.4.: **Dynamic Evolution of the NV State Populations for a Single Laser Pulse (Nanodiamond)**
Here the change in the state populations is simulated for the case of a single laser pulse at saturation intensity (I_{sat}). For simulations the reduced level scheme from figure 2.3 and the parameters from table 2.2 are used. The initial state is given by an equal mixture of the three m_s populations in the 3A2 states. Note that the dashed lines contain the sum over both, the $m_s = -1$ and $m_s = +1$ populations. The Photoluminescence (PL) is the sum of all 3E populations. Both, PL and laser intensity in the top margins of the plot are normalized to 1.

3. Experiment Setup and Methods

In the past decades research on quantum mechanical systems has brought remarkable results. Typically quantum mechanical effects are observed on atomic scale systems, becoming ever harder to detect with growing system size. Some of the most controllable quantum systems are comprised of atoms or ions, which are levitated optically or electrically inside ultra high vacuum. Such experiments often require a long time of planning and building before the first atoms or ions can be captured and manipulated. In contrast, the NV center is a remarkably different kind of quantum system. As it has also been previously discussed (section 2.2), the accessible quantum system of the NV center lives deep within the band gap of diamond. Further the $^3A_2$ ground state is remarkably stable even at high temperatures. In 2019 Herbschleb et al. claimed the highest room temperature electronic coherence time (2.5 ms), of any solid state system [16]. All of this lends the possibility of building a quantum experiment at room temperature under ambient pressure.

This thesis presents the development of a new experimental setup, built from the ground up, designed to explore NV center physics using commercially available nanodiamond particles containing ensembles of NV centers. The details of this setup are discussed in section 3.1. The implementation of readout techniques employed in the setup is described in section 3.2.

This work serves as the first contribution to a larger project that aims to study levitated nanodiamonds hosting NV centers, with the ultimate goal of entangling the spin state of a single NV center to the macroscopic motion of the levitated diamond particle.

3.1. Experimental Setup

The experimental setup is designed to facilitate precise investigations of NV center physics by integrating several key components and techniques. It comprises a confocal microscope (section 3.1.1), with a focus on preparing individual or few nanodiamonds (section 3.1.2), single-photon fluorescence detection (section 3.1.3), and a microwave magnetic field coil for driving spin transitions (section 3.1.4). Experimental control is achieved using the Sinara Artiq framework (section 3.1.5).

3.1.1. Confocal Microscope

A confocal microscope setup is constructed in order to efficiently interface with the NV center optically. Figure 3.1a shows the schematics of this. The microscope uses spatially fixed optics and a movable sample holder. The samples are attached to a glass slide,

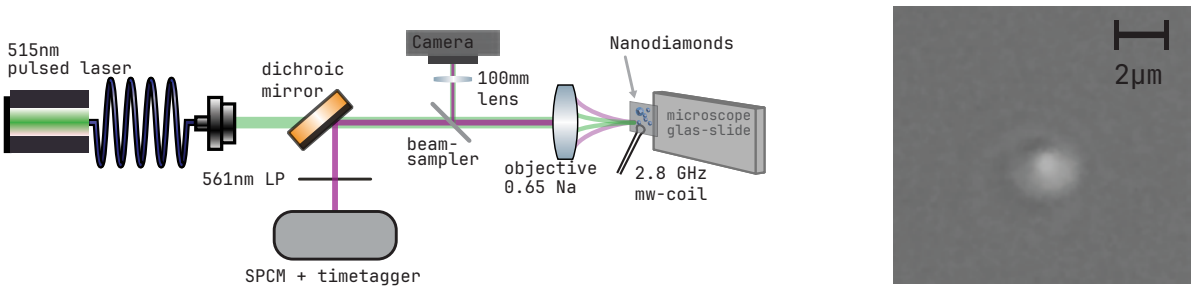

(a) Confocal Microscope Setup (b) Camera Image

Figure 3.1.: **Confocal Microscope Setup**
Diamond particles are prepared in a microscope cover slip sandwich, glued to a glass slide. Fig (a) depicts the confocal setup. A 515 nm TTL-switched (`Cobolt 06-MLD`) laser is used for optical excitation of the NV center. Fluorescence is collected by a `Mitutoyo (0.65 NA)` objective. Red-detuned fluorescence light is separated by a dichroic mirror (556 nm short pass) and filtered through a high quality 561 nm long-pass filter before being detected by a single photon counting module (SPCM: `Excalitas CD3299H`). The SPCM is read out by a `PicoHarp 300` time-tagger. Microwave driving is implemented through a single loop coil positioned right behind the diamond particles. (b) shows an image of the nanodiamond (ND10), which was used throughout most of this thesis. Note that due to the limited resolution of the microscope, the nanodiamond appears much lager in size in the image.

which is screwed to a 3-axis stage. The stage is manually actuated in xyz-direction, by three differential micrometer screws (Mitutoyo) with a 10 µm scale division. A thin-film beam sampler (Thorlabs Pellicle 400-2400nm) together with an achromatic lens of $f = 150$ mm, provides a secondary camera path. For imaging, a microscope camera (KERN ODC874) with the IR filter manually removed, is used as a cost efficient scientific camera in the visible to near-IR light spectrum. A common flexible laptop LED light is used as an incoherent light source for back illumination. This illumination is only used for alignment and is switched off during measurements. Using a calibration target, the camera imaging path was determined to have a magnification of 12 pixel/µm. This ratio is approximately five times the resolution limit of the 0.65 NA objective at green light which is a sufficient oversampling, to not be limited by the spatial-binning effect by the camera's pixels. Figure 3.1b shows an image of the nanodiamond (ND10) used to record much of the data presented in chapter 4 under such incoherent back light illumination. Whether ND10 is a single nanodiamond or a small agglomerate could not be determined.

For optical excitation of the NV centers in the nanodiamond a green 515 nm laser is used (COBOLT-06-MLD). This laser is focused onto the diamond and has a $1/e^2$ near circular beam diameter of 1.60(2) µm. The laser can be modulated via a digital on-off signal (TTL) and has a measured 90:10 rise- and fall-time of 10(1) ns (see figure 3.2) forgoing the need of an AOM for fast switching. Its output power is variable between ≈ 0.5 mW and 45 mW. However, above ~ 3 mW occasional mode hopping is observed, which becomes more frequent with increasing power, leading to a significant fraction of pulses being distorted for power levels above 30 mW. Hence the experiments are performed with a laser power below 3 mW for pulsed sequences throughout this thesis. No further attempts were made to resolve this e.g. by changing the temperature set-point of the laser diode.

3.1.2. Preparation of Nanodiamond Particles

Here an emphasis is given on working with single diamond particles. Unless stated otherwise, all of the measurements presented using nanodiamonds, in this thesis, are the result on measurements performed on a single particle (or small agglomerate). This nanodiamond particle is also referred to as ND10 - this was the first one to provide reliable data.

The nanodiamonds used in this thesis are on average 100 nm in size and supplied by Adámas Nanotechnologies. They specify a concentration of NV centers of 1 to 3 ppm which equates to approximately 300 NV centers within one such Nanodiamond. To prepare single nanometer-sized diamond samples, the nanodiamonds are first dispersed into a diluted suspension using spectroscopic-grade ethanol. The suspension is then subjected to prolonged sonication in an ultrasonic bath, aiming to break up as many agglomerates as possible. Generally, when working with small particle samples in our group (mostly silica spheres), we found that such an ultrasonic bath can indeed break many particle agglomerates. Finally a very small droplet of the suspension is placed directly onto the membrane of an electrical nebulizer. These membranes are vibrated at ultrasonic frequencies creating a very thin mist of droplets shooting up. With some

distance, a thin microscope cover slip is held into the trajectory of the ejected nebula from the nebulizer. This method of creating a very thin mist of a dilute suspension is used to avoid the formation of large 'coffee stain' type of ring containing many particles which are generally formed during the evaporation of droplets containing non evaporating components [35].

Finally, figure 3.1b shows this particle, ND10, imaged under the microscope optically. The setup does not directly allow to distinguish between small agglomerates or single diamond particles directly. However, the lack of resolvable spectroscopic peaks for the four expected NV center orientations (see figure 4.10) could point towards a more polycrystalline arrangement which might either be due to a damaged lattice or an agglomerate of particles.

3.1.3. Photon Detection

The PL of the NV center is detected using a single-photon counting module (SPCM). For pulsed sequences, individual photon "clicks" from the SPCM are time-tagged with a resolution of 4 ps using a time-tagger (`PicoHarp 300`). The `PicoHarp 300` employs a Constant Fraction Discriminator (CFD) input designed to operate under the Nuclear Instrumentation Module (NIM) standard, which requires an input signal ranging from 0 V to −1 V. In contrast, the SPCM (`PerkinElmer CD3299H`) outputs 5 V TTL pulses.

To match these signals, a four-channel detector router (`PicoHarp PHR-402`) is used, which also facilitates triggering. Using this setup, the photon flux time trace is computed by averaging over multiple sequence repetitions.

One important aspect here is that SPCMs only provide a linear response (incoming photon flux vs. outgoing detection pulses) within some limited dynamic range where the lower limit is set by the dark count rate, and the upper by the pulse width and detector dead time. For avalanche photodiode (APD)-based SPCMs, operating beyond this limits can risk damage. This occurs because the internal quenching circuit may fail to properly reset the bias voltage after each detection, potentially leading to a continuous avalanche. Such a prolonged avalanche can cause overheating and damage the APD or its electronics. The SPCM used used within this thesis had a combined pulse and dead time of ≈ 60 ns, indicating a maximum count-rate $\sim 10-20$ MHz. However, for pulsed sequences, a significant distortion to the leading edge is observed at count rates far below this theoretical maximum. Figure 3.2 shows how the initial 100 ns of the same laser pulse are heavily distorted when recorded at a 2 MHz (red) count rate compared to a 200 kHz rate (black), likely due to the detector dead time. For this reason, time-resolved schemes are chosen to be measured at a SPCM count frequency of $\sim 200-600$ kHz only. For steady state measurements (sections 4.3.2 and 4.6) this distortion is negligible when counting over a prolonged time and measurements were often performed at $2-5$ MHz. SPCM count rates are adjusted via additional neutral density filters placed in the photon collection path.

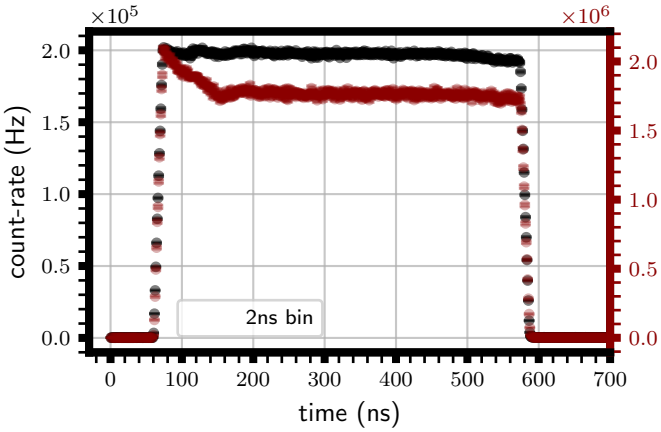

Figure 3.2.: **Signal Distortion at high SPCM count-rate**
Here the laser is set to an output power of 45 mW. The laser output is then attenuated using neutral density filters and directly passed into the SPCM. For the black measurement, an additional neutral density filter is placed in the system, resulting in a $\sim$ 10X lower photon count rate. No other changes to the setup were made between these two measurements. The red dataset consists of 5.4M pulses, the black one was repeated about 238M times. For each, the time-resolved count-rate is plotted with individual y-axes.

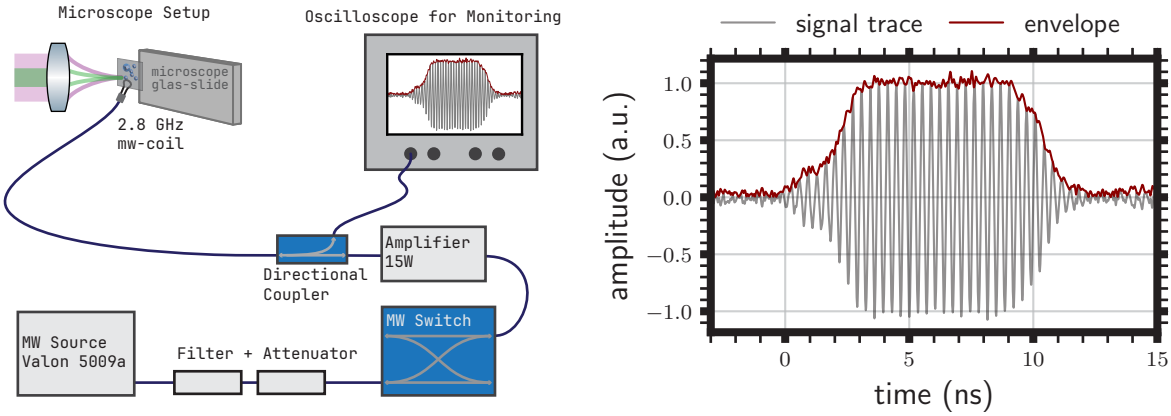

(a) MW Setup Drawing (b) MW Pulse Shape

Figure 3.3.: **Microwave Setup and Microwave Pulse Shape**
(a) Drawing of the MW setup. A directional coupler is used to monitor back reflected MW Pulses from the MW Coil.
(b) Time trace of the reflected MW-Pulse from the MW-Antenna, measured at 40 GS/s. The scheduled length of this Pulse is 10 ns. The pulse-envelope is computed as the absolute of the Hilbert Transformed Pulse yielding a 90:10 rise/fall time of 2.5/2 ns, respectively.

3.1.4. Resonant Microwave Driving

The $m_s = 0$ and $m_s = \pm 1$ projections of the `3A2` ground state are split by a zero-field splitting of 2.87 GHz. These transitions can be driven via a magnetic dipole coupling. In the setup a cost-efficient frequency synthesizer (`Valon 5009a`) is used. Because the bare output of this synthesizer is measured to be comparable to a square-wave signal showing significant higher harmonics in the frequency domain, the signal is filtered by a 2.7 −3.1 GHz band-pass as well as a 5850 MHz low-pass. The signal is amplified with a 15 W amplifier (`Mini-circuits ZHL-15W-422-S+`). This amplifier has the beneficial capability that it can withstand a continuous high back reflection of up to 10 W, relaxing impedance matching constraints on the MW antenna. Pulsed sequences are implemented by switching the synthesizer output (`Mini-Circuits ZASW-2-50DRA+`) using TTL pulses. A directional coupler (`Mini-Circuits ZUDC10-0283-S+`) after the amplifier output was used in reverse to monitor the back-reflection from the MW coil. Back-reflection can occur due to an mismatch between the impedance of the coil and the 50 Ω high frequency RF-cable. Figure 3.3 shows an example trace of such a short mw pulse being reflected back from the MW coil, measured with a fast oscilloscope at 40 GS/s. From the signal trace, the amplitude envelope of the signal is computed as the absolute of the Hilbert transformed signal [36, 37].

3.1.5. Experiment Control with ARTIQ

Fast experimental control was implemented using the open-hardware system Sinara [38] which was assembled for us by Technosystem. The standard Sinara Hardware crate is built around the Kasli core device typically housing an `ARTIX 7` FPGA from XILINX/AMD and custom CPUs handling the FPGA code compilation and communication with an external PC. In a typical configuration the Sinara Hardware crate is built to the Eurocard standard and includes various expansion modules such as `TTL I/O-, DDS-, ADC-, DAC-, AWG-` cards. Sinara is designed to be compatible with the open-source, Advanced Real-Time Infrastructure for Quantum physics (`ARTIQ`) control system for quantum information experiments [39, 40].

Although `ARTIQ` is not a programming language, it provides a Python-based programming environment where users can describe an experiment in Python, which is then executed on FPGA hardware with approximately 1 ns timing accuracy and microsecond latency. This rather neat integration is achieved by separating ordinary Python code (executed on the host pc) from code that is executed on the Sinara FPGA. With this system a given experiment can contain two parts of code. One being actual python code which is executed on the Host PC, the other being functions meant for execution on the FPGA. Such function are written in a syntax closely related to python but are marked with a decorator, `@kernel`. Such a decorator at the function declaration will cause the Python interpreter to invoke the ARTIQ compiler and transform the function's code into a hardware description language executable by the FPGA kernel. The particular usefulness of the ARTIQ framework is that this underlying API handles this communication between the two systems almost seamlessly. A more comprehensive description

of these processes can be found in [39–43]. It should be noted that all experimental code written during this thesis was done so using `ARTIQ-7`, but since June 2024, `ARTIQ-8` has officially been released [44].

Although not elaborated on in this thesis, a variety of coding tools were developed, spanning from general parameterized experiments written in ARTIQ to intermittent, robust data storage and analysis frameworks.

3.2. Experimental Techniques

In section 2.3.4 the spin dependence the PL of the NV was shown and how the NV center's spin state can be polarized. In this section the experimental techniques building on top of these processes are shown.

3.2.1. Pulsed Spin Readout

As described in section 2.3.4, the initial PL of the NV center under a pulsed laser excitation indicates the magnitude of its spin vector at the time of the probe pulse. We can thus use this difference in a pump-probe experiment to effectively read out the NV centers spin state.

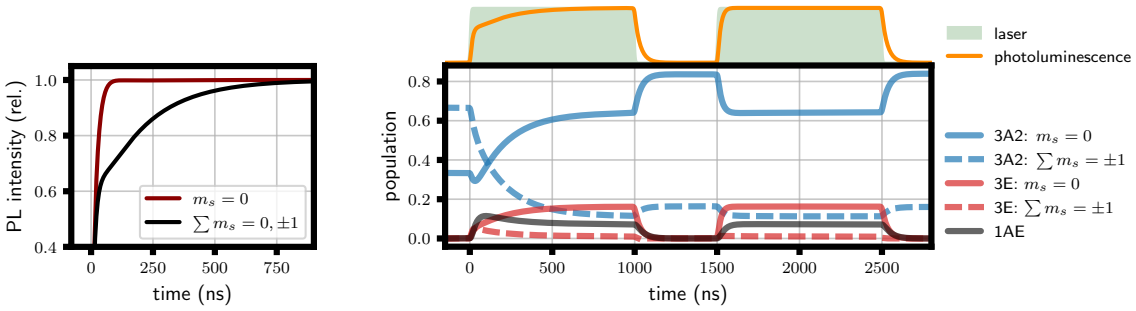

(a) (b)

Figure 3.4.: **Simulation of a Pump-Probe Sequence for Spin Readout**
Simulation of how a pump-probe scheme of two laser pulses can enable spin readout. (a) illustrates the overlap of the initial NV center's photoluminescence signals for two sequential laser pulses. (b) depicts the temporal profile of these laser pulses along with the corresponding changes in the NV center's state populations. The PL is calculated by summing over the populations in the `3E` state manifold. The simulation is performed for a laser intensity of $\frac{3}{4} I_{\text{sat}}$.

In figure 3.4b such a pump-probe sequence is simulated using the parameters from table 2.2. There, the laser pulses and PL are drawn in the top margin. These laser pulses are scheduled sequentially and are 1 µs long each, with a delay of 500 ns in between them. In figure 3.4a the initial normalized PL expected for the two pulses is overlayed

temporally. The black line shows the expected PL for an NV center starting in an initial mixed spin state, while the red line shows the PL of the second pulse where the NV center's spin has already been polarized into the $m_s = 0$ spin by approx. 84 %. Here a clear difference is observable, in that the initial PL of a previously polarized NV center is significantly greater. This phenomenon of spin dependent PL can be explained by observing the population dynamics of the `1AE` manifold which is a dark state in figure 3.4b (black line). For the first pulse, the `1AE` population rises significantly before stabilizing at a steady state. By contrast, during the second pulse, the $m_s = \pm 1$ population in the `3A2` ground state is reduced, resulting in a smaller `1AE` population that does not overshoot as it did during the first pulse. Consequently, equilibrium is reached more quickly in the second pulse.

Let us now compare this to an experimental realization of such a sequence. For the experiment such a pump-probe sequence was repeated 41M times in order to gather sufficient data. Between each sequence repetition a wait time of 5 ms was introduced such that the resulting polarized spin state had a sufficient time to decay back into a thermal mixture. Similarly to figure 3.4a a PL trace is computed by binning the arriving photons and overlaying the resulting histograms. This can be seen in figure 3.5a. The Figure 3.5b shows in black the magnitude of this luminosity difference.

We will now use these two photoluminescence curves to extract a dimensionless signal from them. Instead of taking the initial PL directly or their difference, we will compute the visibility of this contrast in the following way.

$$\mathrm{vis}(t) = \frac{S_{\mathrm{Pump}}(t) - S_{\mathrm{Probe}}(t)}{S_{\mathrm{Pump}}(t) + S_{\mathrm{Probe}}(t)} \tag{3.1}$$

Here $S_{\mathrm{Pump/Probe}}(t)$ is the total number of photons collected within the time interval $[0, t]$ as can be written as

$$S_i(t) = \int_0^t \mathrm{PL}_i(t')dt'.$$

This visibility signal is chosen because it is dimensionless and thus independent of slow PL drifts (compared to the Pump-Probe sequence time) caused by fluctuations. Because an SPCM is used to record $\mathrm{PL}(t)$, the error of S_i is mainly given by shot noise ($\Delta S_i = \sqrt{S_i}$), and therefore the error of $\mathrm{vis}(t)$ is can be written as

$$\Delta\mathrm{vis}(t) = 2 \cdot \sqrt{\frac{S_{\mathrm{Pump}} S_{\mathrm{Probe}}}{(S_{\mathrm{Pump}} + S_{\mathrm{Probe}})^3}}. \tag{3.2}$$

We can now compute the signal to noise ratio (SNR) as

$$\mathrm{SNR(t)} = \mathrm{vis}(t)/\Delta\mathrm{vis}(t) \tag{3.3}$$

to find the optimal integration window $[0, t]$, which is given as the maximum of equation (3.3), for which we gain the best spin readout signal. In figure 3.5b the two curves of $\mathrm{vis}(t)$ and SNR(t) are plotted. Here, the visibility is shown in blue with the shaded area surrounding the line indicating the $\pm 1\,\sigma$ error region. The SNR(t) (purple curve)

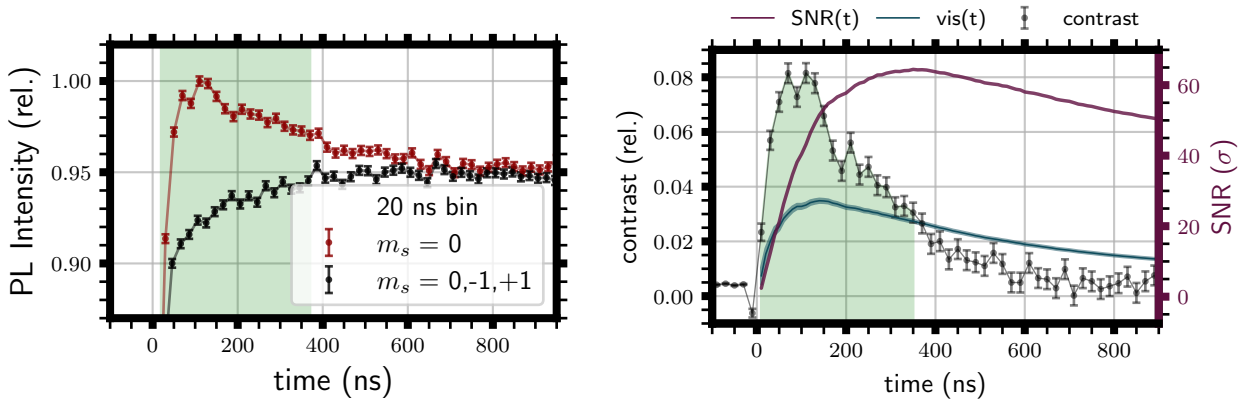

(a) (b)

Figure 3.5.: **Spin Readout Signal**
Here the PL of a pump-probe sequence with two 1 µs long laser pulses at $\approx \frac{3}{4} I_{\text{sat}}$ is recorded. The Pump Pulse leaves the NV center's spin polarized, leading to a different PL at the beginning of the Probe Pulse. In (a) this difference is shown as the two PL traces of the Pump and Probe pulse are overlayed. The black data is for the pump pulse where the NV center is initially in a thermal spin mixture of $m_s = 0, +1, -1$. Compared to this the red data shows the probe pulse where the NV center's spin has now been polarized into the $m_s = 0$ state by the pump pulse. In (b) the difference between in PL (probe - pump) from (a) is plotted in black. In blue, on the same y-axis, the time dependent visibility according to the negative of equation (3.1) is shown. Finally on a separate y-axis the SNR(t) (equation (3.3)) shows the signal-to-noise-ratio for a varying integration time t.

has a maximum at 350 ns. This corresponds to an optimum integration region of 0 to 350 ns, at which a visibility of 0.00274(4) is measured.

In the following, this optimum integration time window will be used throughout the thesis (sections 4.5 and 4.7) to obtain an optimized visibility value. Note that the visibility in figure 3.5b actually corresponds to the negative value of equation (3.1). This is because in later experiments it will be more time efficient and stable to introduce an extra pump pulse at the beginning of the sequence, as will be discussed later (see also figures 4.7 and 4.11).

3.2.2. Optically Detected Magnetic Resonance Spectroscopy

In addition to the spin readout method described above, which allows for measuring changes in the NV center's spin polarization over time, another widely used technique for probing spin properties with optical excitation is optically detected magnetic resonance spectroscopy (ODMR). ODMR shares conceptual similarities with the well-established technique of electron paramagnetic resonance (EPR) spectroscopy commonly used in material science.

Both rely on the fact that transitions between spin sublevel can be driven via magnetic dipole coupling by applying a resonantly oscillating magnetic field (at MW frequencies). In the context of the NV center, if the driven spin flip is either the $m_s = 0 \rightarrow m_s = -1$ or $m_s = 0 \rightarrow m_s = -1$ transition then again the difference in PL between the $m_s = 0$ and $m_s = \pm 1$ manifold can be employed. Compared to section 3.2.1 of time resolved readout here, two steady state cases can be differentiated. The first case is when an oscillating magnetic field is off-resonant to the $m_s = 0 \leftrightarrow m_s = 1, -1$ transition in which case the NV center is continuously being polarized into the $m_s = 0$ state and has a high PL.

In the second case, the MW frequency is resonant to this transition, then the $m_s = +1$ or -1 spin state will be become populated, in turn leading to a greater population of `1AE` thus lowering the PL. If the mw driving is sufficiently strong compared to the optical driving, then scanning the driving MW frequency over a frequency range where such resonances lie will reveal characteristic dips in the steady-state photoluminescence whenever the driving MW field comes into resonance with either the $m_s = 0 \rightarrow m_s = -1$ or $m_s = 0 \rightarrow m_s = -1$ transition. This technique is employed in section 4.6.

4. Results and Measurements

In chapters 2 and 3 the theoretical background and the experimental tools for manipulation, readout and sensing are introduced. In this chapter the current state of measurement and manipulation techniques regarding NV center doped diamond particles within our group is shown. The results of sections 4.2, 4.4, 4.5 and 4.7 are used to inform the decay rates of the simulation model for nanodiamonds. The results in section 4.6 shows two examples of NV center sensing applications such as determining the orientation of small diamond particles and the absolute temperature of the particle.

4.1. Fluorescence Spectrum

Measuring the spin dependent PL serves as the basis of all readout schemes used during this thesis. This PL is the result of integrating over a spectral range of wavelengths $\lambda \in [561, \approx 1000]$nm. The lower bound is set by a 561 nm cutoff long pass filter in order to filter out elastic scattered laser light at 515 nm and the upper wavelength limit is given by the SPCM sensitivity.

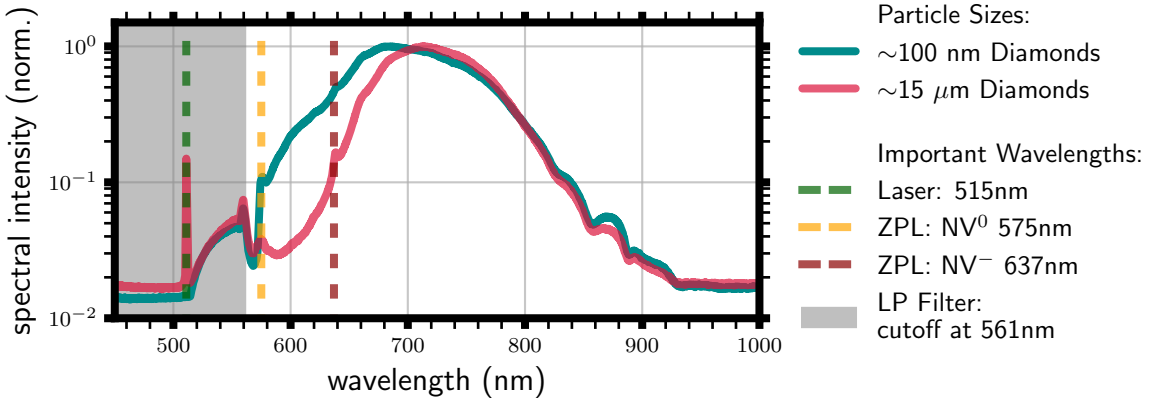

Figure 4.1.: **Spectral Intensity of NV center Photoluminescence**:
The relative spectral intensity of the NV center's photoluminescence is measured for nanometer (blue) and micrometer (red) sized diamond particles. Vertical lines mark the laser wavelength (515 nm) as well as the $\mathtt{NV}^-$ and $\mathtt{NV}^0$ zero phonon lines (637 and 575 nm). The gray area shows the spectral part which is blocked by a Semroc 561 nm Long-pass (LP) filter. As the cut-off wavelength of the dichroic mirror seen in figure 3.1a is below the LP filter, it is not drawn here.

Figure 4.1 shows the spectral intensity of the Photoluminescence collected from NV centers for two different particle sizes. For the nanometer sized particle measurement, an ensemble of particles was measured. The photoluminescence light is filtered by a 561 nm long-pass filter and sent to a spectrometer (`Andor Kymera 193i`) via a multi-mode fiber. Because the 515 nm excitation laser off-resonantly excites both the $\mathtt{NV}^-$ as well as the $\mathtt{NV}^0$ charge state of the NV center, it is expected that for an ensemble of NV centers to find both charge states contributing to the fluorescence. This can also be qualitatively observed in the spectrum, by the increase in fluorescence right at the $\mathtt{NV}^0$ ZPL line. Between the $\mathtt{NV}^0$ and the $\mathtt{NV}^-$ ZPL lines, mostly the $\mathtt{NV}^0$ stokes sideband contributes, where as for wavelengths larger than the $\mathtt{NV}^-$ ZPL the stokes sidebands from both charge states are present.

It is further observed that the normalized spectrum measured with nanometer sized diamond particles appears significantly shifted towards shorter wavelengths. This could be due to two reasons. Firstly: the increase at the $\mathtt{NV}^0$ ZPL line is more pronounced in the NV center spectrum of nanometer sized diamonds compared to the spectrum of micrometer sized diamond particles. Secondly as it is discussed in section 2.2.3, a greater suppression of optical emission in very small (compared to the emission wavelength) diamond particles is expected. Such a suppression, for diamonds that are about as large as the optical wavelength inside the diamond, is not necessarily uniform over the wavelength range and could suppress longer wavelength emission stronger. Because in figure 4.1 the intensity is normalized to the maximum of each curve, such a disproportionate suppression would also shift the observed spectral peak towards shorter wavelengths.

It is assumed, that this $\mathtt{NV}^0$ contribution adds a constant offset to the PL. While for single NV centers charge conversion and checking protocols [27] offer the possibility to filter out the $\mathtt{NV}^0$ contribution, for the ensembles used here this is likely not feasible and thus contributes to the background noise.

4.2. Radiative Decay Rate

A great deal of the optical initialization and readout process as used throughout this thesis depends on the spin selective intersystem crossing rates, ISC. This was mentioned in section 2.3.4, leading to the spin readout presented in section 3.2.1 but also the physical observation of section 3.2.2. In section 2.2.3 it is shown how this fundamental process is different in the case of nanodiamonds containing NV centers. In this section I aim to determine an optical emission rate by measuring the decay of observed PL by taking into account literature values for the phonon relaxation process.

With off-resonant driving at 515 nm, the measured PL will be the sum of the contributions from all spin states in the `3E` manifold. Under continuous driving an equilibrium of constant spin mixing and spin polarization is reached (figure 2.4). We now consider the case when the driving laser is switched off. Solving the optical Bloch equations (equations (A.4) and (2.19)) for the five level scheme presented in figure 2.3 will result

in an exponential decay of each spin state with a rate of

$$\gamma_{|2\rangle}^{\text{dec}} = \gamma_{20} + \gamma_{24} \quad \text{and} \quad \gamma_{|3\rangle}^{\text{dec}} = \gamma_{31} + \gamma_{34} \tag{4.1}$$

for the $m_s = 0$ (state $|2\rangle$) and $m_s = \pm 1$ (state $|3\rangle$) spin states of 3E respectively. The observed decay from the 3E manifold is then proportional to a weighted sum over the two decay channels such that the normalized observed PL becomes

$$\text{PL}(t) = \epsilon e^{-\gamma_{|2\rangle}^{\text{dec}} t} + (1-\epsilon) e^{-\gamma_{|3\rangle}^{\text{dec}} t}. \tag{4.2}$$

Here ϵ is the degree of polarization into the 3E $m_s = 0$ state ($|2\rangle$), reached in the steady state equilibrium, which is defined as

$$\epsilon = \frac{\rho_{22}}{\rho_{22} + \rho_{33}} \tag{4.3}$$

where ρ_{22} is the population of the $|2\rangle$ state (3E $m_s = 0$) and ρ_{33} the population of state $|3\rangle$ (corresponding to the sum of the $m_s = \pm 1$ populations of 3E) at the moment the laser is switched off.

It is often reported that the optical decay rates should be equal for the different spin states of 3E [6], i.e. $\gamma_{20} = \gamma_{31}$. Still, from equation (4.2) we would then have to determine four individual parameters just from measuring the observed PL curve corresponding to this decay. Such an effort would likely not yield any useful results. Thus, literature values for the ISC crossing rates are used. For this, a focus is given on experiments that have reported individual values of decay rates.

Reference	γ_{20}, γ_{31} 3E →3A2	γ_{24} 3E $_{m_s=0}$ → 1AE	γ_{34} 3E $_{m_s=\pm1}$ → 1AE	Note
Robledo [21]	65	11	80	HTHP bulk, RT
Ernst [14]	49(7)			CVD Nanopillars, cryo
Gupta [22]	66.8(7)	10.5(7)	90.8(15)	CVD bulk, RT
Tetienne [23]	66(3)	8(2)	53(5)	CVD bulk, RT
[14, 21–23] Avg. ± std.	62 ± 7	9.8 ± 1.3	75 ± 16	

Table 4.1.: **Reported Transition Rates in MHz:**
All of these results have been obtained from individual NV centers. The different measurement circumstances are noted: Room Temperature (RT), cryogenic temperature (cryo), High Temperature High Pressure (HTHP), Chemical Vapor Deposition (CVD). Bulk refers to a diamond that is much larger than the optical wavelength. In case multiple NV centers have been measured, the average(± std.) is quoted here. The average of these rates is used for simulation parameters (see table 2.2). Because the measurement resulting in the non-radiative rates by [14] are performed at cryogenic temperatures, they are not used here.

Table 4.1 gives an overview of a number of reported NV center transition rates in literature. One commonality between all of the measured quantities is that they are performed on individual NV centers, usually housed inside a high-grade bulk diamond. Ernst et al. [14] being the only exception here: they measure their NV properties in Nano-pillars etched into a CVD diamond sample, the pillars themselves are reasonably large compared to the fluorescence wavelength as they detail in [45]. Nevertheless they do measure a slight reduction in the optical emission rate. For the simulation, the average of the reported ISC rates in table 4.1 ($\gamma_{24} = 9.8\,\text{MHz}$, and $\gamma_{34} = 74\,\text{MHz}$) is used.

We now compare these to the experimental observations. Figure 4.2a shows this measured on an approximately 15 µm sized diamond while figure 4.2b shows this measured in an approximately 100 nm sized diamond. A double exponential decay would be expected according to equation (4.2). However the decay can only be reliably fitted after the excitation laser has been fully turned off (in figure 4.2b this laser is plotted in shaded green, a falling edge of 10 ns has been measured, see also figure 3.2). Hence the fit is only 16 ns started after the laser has been switched off. Here we observe a good match to a single exponential fit. This is expected because by that time, the lesser populated state $|3\rangle$, which also has a much greater ISC rate ($\gamma_{34} = 75\,\text{MHz}$), will have decayed almost entirely. This behaviour can be recreated by the simulation shown in figure 4.2c. In this figure, the simulated PL and the two simulated excited state populations, which add up to this simulated PL, are overlayed with the data from figure 4.2b. For the simulation a measured laser pulse shape is used, which is drawn in shaded green. We can observe in this case that the simulated PL very closely follows the population of the state $|2\rangle$ (^3E $m_s = 0$). A single exponential fit performed on this simulated PL, also started 16 ns after the laser has been switched off, yields the same exponential lifetime as the value obtained in figure 4.2b. Therefore $\gamma^{\text{dec}}_{|2\rangle} = \frac{1}{\tau_{\text{dec}}}$. Following equation (4.1) the optical decay rate is obtained as

$$\gamma_{20} = \gamma^{\text{dec}}_{|2\rangle} - \gamma_{24} = 19.5\,\text{MHz}.$$

This value is significantly lower than the expected decay rates in bulk diamond as quoted in table 4.1. We expect this to happen due to the suppression of optical emission (section 2.2.3). The measured value here corresponds to a suppression of optical decay by a factor of 3.3. This agrees reasonably well with the rough estimate of a suppression by a factor of 4.2 (equation (2.11)) derived in section 2.2.3.

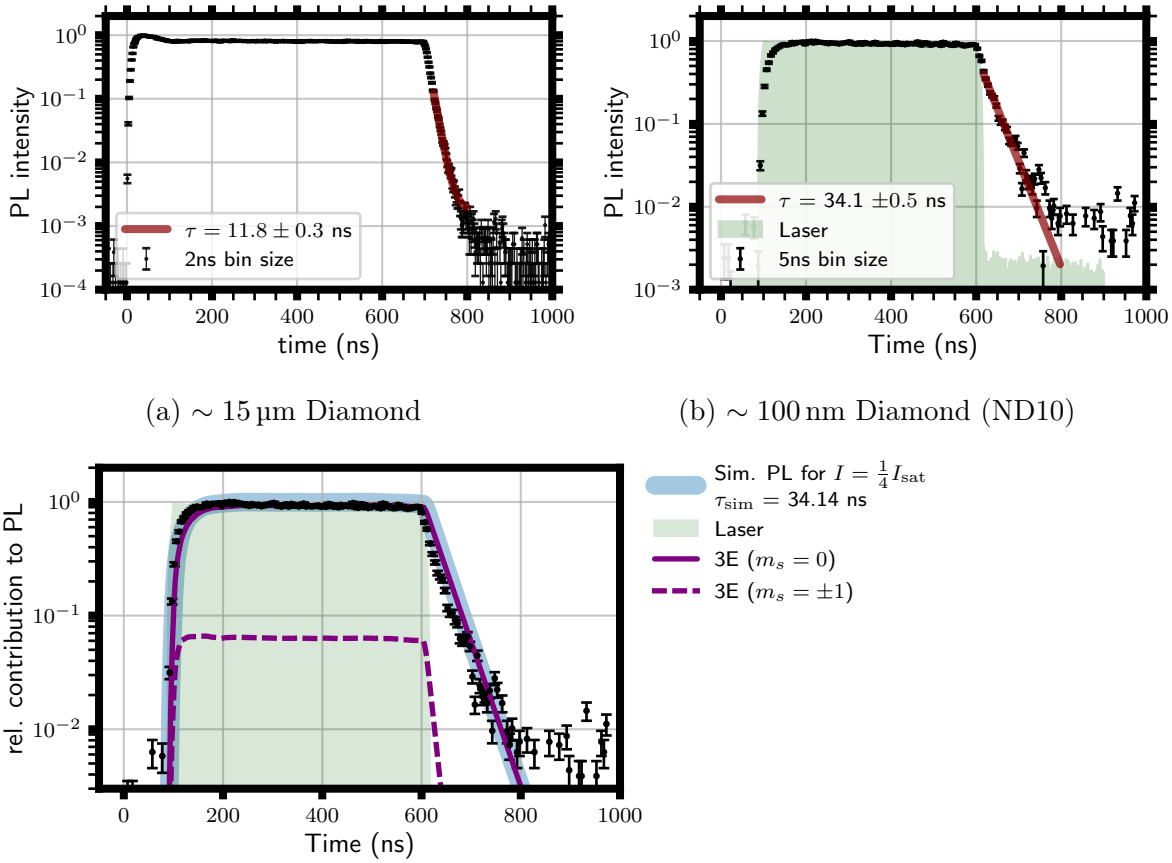

(a) $\sim 15\,\mu$m Diamond

(b) $\sim 100\,$nm Diamond (ND10)

(c) $\sim 100\,$nm Diamond - Simulation

Figure 4.2.: **Radiative Decay of the 3E Excited State**
Pulse shapes are measured by integrating the photoluminescence observed as an average for a rapidly repeated sequence. Two different host diamond particles are measured. (a) shows the PL for a 700 ns pulse on a single $\sim 15\,\mu$m sized diamond with the laser spot size smaller than the diamond. In (b), (c) the recorded PL for a 500 ns pulse-sequence of a Nanodiamond (ND10) is shown, here the same sequence was repeated with the excitation laser being $\sim 5\,\mu$m displaced from the diamond to get a background which is subtracted from the measurement. A single exponential fit, which is only started 16 ns after the laser pulse has been switched off, is used to obtain the decay time τ_{dec}. (c) depicts the same data as in (b) but is expanded with a simulated PL as well as the time evolution of the state populations of the excited states. The simulation was performed at $\frac{1}{4} I_{sat}$ which corresponds to the laser intensity used in the experiment shown in (b). For the simulation a separately measured reference laser pulse shape similar to figure 3.2 was used which is drawn in shaded green.

4.3. Optical Saturation

For all the simulations of NV center dynamics so far used, the coupling strength of the laser, Ω, is always given in units of the saturation intensity I_{sat}. For the spin polarization simulation in figure 2.4 this was at 1x I_{sat}, for the spin readout of figure 3.5 at $\frac{3}{4}I_{\text{sat}}$ and for the previous simulation of the decaying PL, figure 4.2, a value of $\frac{1}{4}I_{\text{sat}}$ was used. In the latter two cases, these values where chosen to correspond with the laser power used for each of these experiments. In this section the implicitly referenced saturation measurement allowing this determination of the laser coupling strength is presented. Firstly, in section 4.3.1, the saturation behavior of the NV center's multilevel system is compared to that of a quantum two-level system, highlighting how a strongly illuminated NV center exhibits similar saturation characteristics to a two-level system. Subsequently, in section 4.3.2, the NV center's saturation curve is measured.

4.3.1. Simulating the Optical Saturation of the Nitrogen-Vacancy Center

In a two level quantum system that is driven with a resonant laser, the amount of photoluminescent light, $\text{PL}(I)$, emitted, depends on the laser intensity (I) as

$$\text{PL}(I) = \text{PL}_{\text{max}} \frac{I}{I + I_{\text{sat}}}. \tag{4.4}$$

Here PL_{max} is a constant factor that corresponds to the maximum PL which would be emitted at infinite driving power. The parameter I_{sat} is called the saturation intensity, at which the observed PL will no longer be linearly dependent on the laser power but start to plateau.

A similar equation to equation (4.4) can also be obtained from solving the master equation (equation (2.19)). This, in the case of a two level system being resonantly driven at rate Ω leads to following equation for its excited state population ρ_{ee} (the full calculations can be found in Section A.1)

$$\rho_{ee} = \frac{1}{2} \frac{\Omega^2}{\Omega^2 + \frac{\Gamma(\Gamma+\xi)}{2}}. \tag{4.5}$$

In this equation Γ denotes the decay rate from the excited state $|e\rangle$ to the ground state $|g\rangle$, and ξ the rate of dephasing of the excited state $|e\rangle$. We can now identify a saturation parameter Ω_{sat} as

$$\Omega_{\text{sat}}^2 = \frac{\Gamma(\Gamma + \xi)}{2}. \tag{4.6}$$

Because the rabi frequency squared (Ω^2) is proportional to the laser intensity, I, we can then write

$$\frac{I}{I_{\text{sat}}} = \frac{\Omega^2}{\Omega_{\text{sat}}^2}$$

allowing us to obtain the rabi frequency as a function of laser intensity I through

$$\Omega(I) = \sqrt{\frac{I}{I_{\text{sat}}} \times \frac{\Gamma(\Gamma + \xi)}{2}}. \tag{4.7}$$

Let us now turn to the fact that the reduced level scheme of $\texttt{NV}^-$ (figure 2.3) which is used for the simulation is not a two level system. The most relevant differences are the two excited and ground states ($m_s = 0, \pm 1$) of `3A2` and `3E` which mix via the intermediary singlet levels subsumed in `1AE` .

We can however approximate an equation similar to equation (4.7) which reasonably estimates Ω based on the laser intensity by using a slightly modified decay parameter Γ'

$$\Omega(I) = \sqrt{\frac{I}{I_{\text{sat}}} \times \frac{\Gamma'(\Gamma' + \xi)}{2}} \tag{4.8}$$

where Γ' is defined as

$$\Gamma' = \epsilon \left(\gamma_{20} + 1/\left(\frac{1}{\gamma_{24}} + \frac{1}{\gamma_{40}} \right) \right) + (1 - \epsilon) \left(\gamma_{31} + 1/\left(\frac{1}{\gamma_{34}} + \frac{1}{\gamma_{41}} \right) \right). \tag{4.9}$$

Here ϵ denotes the polarization of the `3E` excited state defined in equation (4.3).

This polarization is used to weight the contribution to the PL of each state. In absence of direct measurement methods, ϵ is determined by running the simulation first. The rates γ_{20} and γ_{31} correspond then to the direct optical channel while the inverse sum of the rates $(\gamma_{24}, \gamma_{40})$ and $(\gamma_{34}, \gamma_{41})$ account for the fact that the second channel via the ISC consists of two sequential decay processes.

In figure 4.3 a simulation of the NV system is shown. Here compared to the previous simulations, the steady state is directly computed using Source Code 2. From this simulation, two observations are made: Firstly, the degree of polarization of $|2\rangle$ which is drawn in green remains almost independent of the driving intensity. This justifies the previous approach of using a constant polarization ratio to determine Γ'. Secondly, if the equation (4.4) is freely fitted to the numerical results of the simulation in figure 4.3, we obtain a value of $\Omega_{\text{sat}} = 1.04$. Given fact that the x-axis is normalized by units of Ω_{sat} a value of 1 would be expected. This is only a slight deviation from this expectation. If necessary the value Ω_{sat} could be multiplied by this deviation to obtain a more accurate fit. It should be noted that equation (4.7) using the parameter Γ' is not always an accurate solution to to the saturation intensity of the described five level system. It rather provides an initial guess which can be verified by running the simulation seen in figure 4.3. If larger deviations on the fitted saturation value are observed, the estimate of I_{sat} may be updated with the result of the simulation

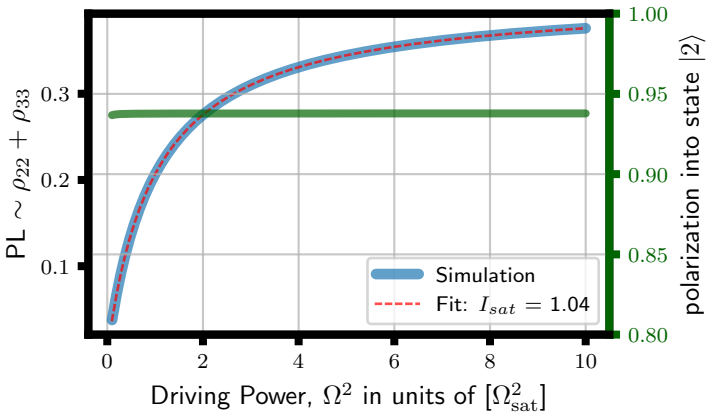

Figure 4.3.: **Simulation of the Steady State vs Driving Power**
The steady state equilibrium of the driven NV system as defined in section 2.3 is simulated as a function of Ω^2, the rabi frequency squared which is proportional to a laser intensity in experiments. The driving frequency is modeled as resonant to the transition. The x-axis is given in units of the saturation parameter Ω^2_{sat} defined in equation (4.6). The left y-axis is the sum of the steady state excited state populations of the `3E` which is proportional to an observed photoluminescence in experiments. The right y-axis (green) corresponds to the polarization of the state $|0\rangle$ reached in the steady state equilibrium.

4.3.2. Measured Optical Saturation

Let us now turn to the measured optical saturation. This is shown in figure 4.4b, where the PL of ND10 is measured as a function of the illuminating laser power.

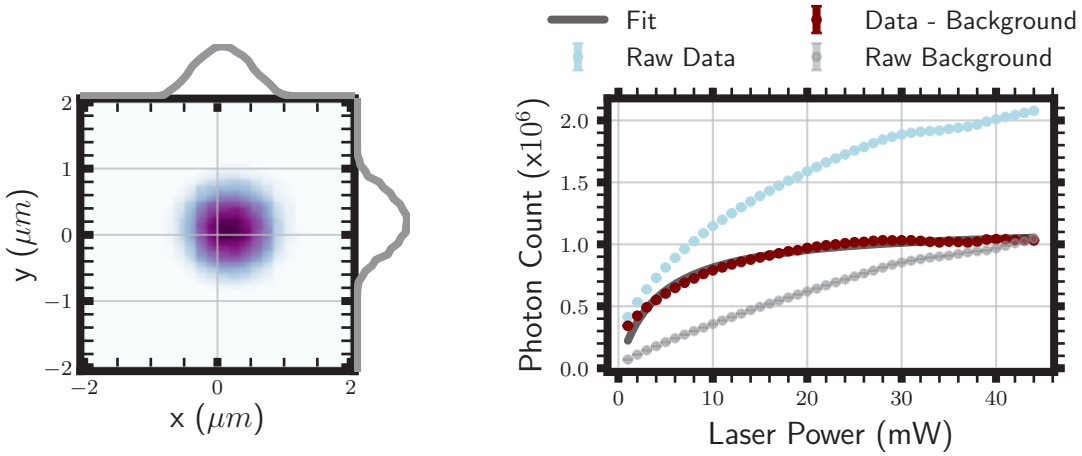

(a) Intensity Profile

(b) Measured Saturation

Figure 4.4.: **Optical saturation of ND10:**
Saturation intensity of the nanometer sized diamond ND10 is measured. (a) shows the intensity profile of the focused laser spot. This is recorded via the imaging system drawn in figure 3.1a. The one dimensional intensity profile of the laser spot, along the x and y axis, is shown in the top and right margin of the figure respectively. In (b) the recorded PL (blue) as a function of the set laser power is shown. A significant background contribution (gray) was observed by repeating the measurement approximately 5 µm next to the nanodiamond. This background is subtracted from the PL of ND10 resulting in the data (red). Fitting equation (4.4) to this data yields a saturation power of $P_{\text{sat}} = 4.2(2)\text{mW}$.

Firstly we observe a large contribution of the background, which can be seen in the gray curve. The background signal is measured by performing the same sequence with the confocal microscope focused next to ND10 with a displacement of approximately 5 µm. By subtracting this background contribution we find a fairly good agreement with a saturation fit to equation (4.4) (solid black line) yielding a set laser power of 4.2(2) mW, at which saturation is reached. Here, to obtain the actual transmitted power, this value is scaled by the transmission factor of the setup, which was measured to $T = 0.685$. Deviations from the fit at the higher and lower power range are attributed to fluctuations in the laser intensity, which was only set via a software command and not monitored separately. The main source of error for this measurement likely comes from the alignment of the confocal microscope setup itself. By fitting a gaussian function to the x and y intensity curve shown in the top and right margin (gray) in figure 4.4a, a $1/e^2$ diameter (equal to 4σ) of 1.60(2) µm is obtained. In the experiment, the laser beam

is aligned to be centered on the approximately 100 nm sized diamond by maximizing the amount of PL recorded.

In order to derive an estimate of the actual saturation intensity, we will calculate the average laser intensity, seen by the much smaller nanodiamond, given some error in alignment of the nanodiamond's position with respect to the laser beam center. As mentioned in section 3.1.1, the minimum screw division of the differential micrometer screws, used for positioning of the nanodiamond, 10 µm. This scale division is much larger than the positional accuracy to which the nanodiamond can be aligned. We thus derive an estimate of the alignment error based on the qualitative observation that the observed PL after alignment seems to lie within $60 - 100\,\%$ of the maximum PL. This would correspond to a $\pm 1\sigma$ misalignment of the nanodiamond's position with respect to laser beam center. For simplicity here, we can assume that the diamond is much smaller than the laser beam and the PL is linear to the illuminating laser intensity. Then the average laser intensity incident in this are will be given by

$$I_{\text{avg}} = \frac{0.68\text{T}P_{\text{Laser}}}{\pi\sigma^2}. \tag{4.10}$$

where $T = 0.685$ is the measured total transmission, and the factor 0.68 arises from integrating a normal distribution over the range $[-\sigma, \sigma]$, representing the fraction of the total laser power contained within a circular area of radius σ around the beam center. This results in an estimated saturation intensity of $I_{\text{sat}} = 390\,\text{kW}\,\text{cm}^{-2}$. Doing a similar calculation with a misalignment of $2\sigma = \pm 800\,\text{nm}$, would on average result in $I_{\text{sat}} = 136\,\text{kW}\,\text{cm}^{-2}$. Thus this saturation intensity has a large error bar. According to [25], the average observed saturation intensity for nanodiamonds hosting NV center ensembles is $70(15)\,\text{kW}^2\,\text{cm}^{-1}$.

4.4. Lifetime of the Singlet States Manifold

As it has been discussed in many parts of this thesis, the intersystem crossings play a crucial role in the NV center's dynamics. In section 4.2 a focus was given to the first ISC, namely the transition from the excited `3E` into the `1A1` , `1E` manifold. Here an emphasis is given to the second part of this ISC, the transition out of this singlet manifold into the `3A2` ground state. For simplicity again the `1A1` and `1E` state are combined into one effective `1A1` (see also figure 2.3). Note that the transition `1A1` $\rightarrow$ `1E` is dipole allowed and photo-emission from that transition has been observed [21], but given that the SPCM used in this thesis is not sensitive at this wavelength of $\approx 1042\,\text{nm}$, all the time the NV spends in this singlet manifold can be treated as a dark state.

Let us now turn to the measured lifetime of this dark state. This can be achieved indirectly via a pump probe sequence. In figure 2.4 it is shown how the PL in the beginning of a pulsed illumination is indicative to some of the state populations at the beginning of the pulse start. In section 3.2.1 this was used to measure the polarization of the `3A2` spin states by comparing these initial PL for a spin polarized case and thermal spin mixture. Here, a similar pump-probe experiment was performed, but with a much shorter

delay in between the two pulses. The schematics of this is shown in figure 4.5b depicting a simulation of the dynamical change in the NV center's PL. Figure 4.5b focuses on the region where the pump pulse ends and the probe pulse begins. There the relevant dynamics are captured by the decay of the `1AE` state drawn in black. Under sufficient laser illumination during the pump pulse, the system quickly enters into a steady state equilibrium between the radiative triplet manifold and dark singlet state. This equilibrium between NV centers being pumped into, and decaying out of the `1AE` states has an overall lower photoluminescence compared to the system being left undisturbed long enough for the NV to fully decay into its ground state. After the illumination ends, the `1AE` state decays into the `3A2` manifold. If now the probe pulse is scheduled before the `1AE` state has been fully depleted, the steady state solution is reached immediately and the observed PL stays low. This difference in initial PL is shown in figure 4.5a.

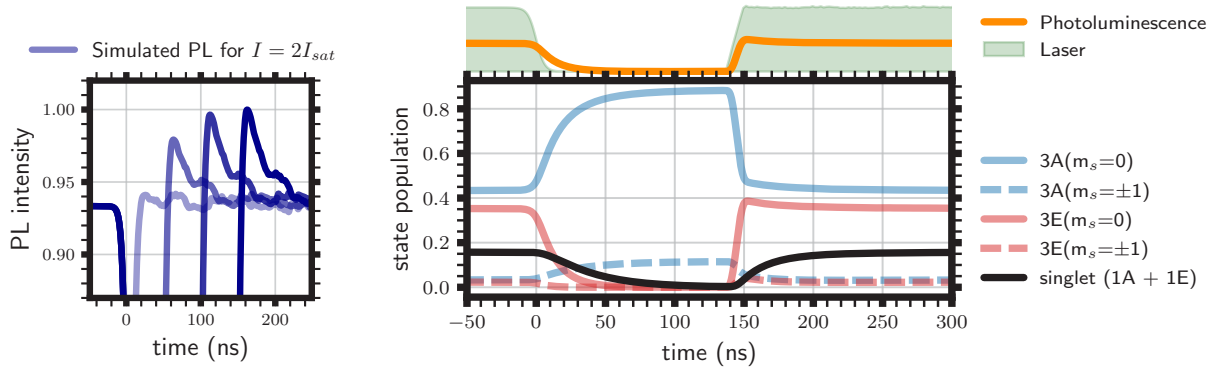

(a) (b)

Figure 4.5.: **Lifetime of the Singlet State Simulation**
A simulation at $2I_{\text{sat}}$ is performed to show the effect of the 'dark' singlet `1AE` manifold on the PL in a pump-probe measurement sequence. (b) shows the dynamical changes in populations under a pump probe measurement scheme. The laser pulses are again shown in the top margin of the plot, for the leading edge of the second pulse, a real laser pulse is used. Because this simulation aims to explain a measurement performed on a microdiamond an optical decay rate of 62 MHz is used which is expected for large microdiamonds. In (a) the resulting PL is plotted for four different delays between the pump and probe pulse of 10, 50, 100 and 150 ns.

Next, this simulation is compared to an experimental measurement performed on a micrometer-sized diamond containing ensembles of NV centers, as shown in figure 4.6. In this measurement, two laser pulses of 700 ns each are applied in rapid succession, with the delay between pulses varying from 0 to 400 ns. The PL is recorded across many repetitions of the same sequence. In figure 4.6a, five example PL traces are displayed for different pump-probe pulse delays. It is evident that for short delays, the initial PL of the probe pulse reaches only the steady-state equilibrium. In contrast, sequences with longer delays exhibit a distinct initial peak.

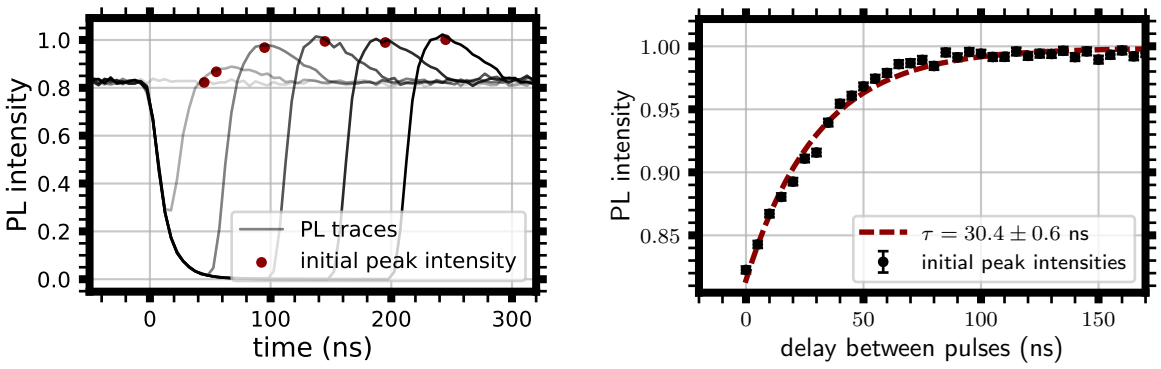

(a) (b)

Figure 4.6.: **Observed Recovery of an Initial PL Peak, Pointing Towards a Singlet State Lifetime (Microdiamond)**
The recovery of initial PL is measured as a function of wait time between a polarizing pump and a readout probe pulse, each 700 ns long. Compared to previous measurements, here a $\sim 15\,\mu$m sized diamond (Microdiamond) is used. (a) shows six example PL traces measured with Pump Probe delays of $[10, 50, 100, 150, 200]$ns. The red dots are the mean values computed from the first (30 - 60)ns of the Probe pulse. (b) shows these computed mean values of the initial peak PL for all measured pump probe delays from 0 to 400 ns. Beyond 150 ns this curve remains constant, thus only the data in the first 150 ns is shown. A single exponential function is fitted to the data to determine a time constant of $\tau = 30.4(6)$ ns.

A measure of this peak is computed as the mean PL from the first $30 - 60$ ns after the probe pulse has been switched on. These peaks are plotted as red dots in figure 4.6a. In figure 4.6b these computed peaks are plotted for all of the measured pump probe delay values where an exponential fit yields a time constant of $\tau = 30.4(6)$ ns.

This time constant is attributed to the combined lifetime of the singlet states, however this value does not agree with other lifetime constants reported in literature. For bulk material this lifetime has been consistently measured in the range of $145 - 175$ ns at room temperature [21, 22].

Although this lifetime is known to decrease with rising temperatures due to stimulated phonon emission from thermal excitations, such a temperature increase is unlikely in this case. The measurement in figure 4.6 was conducted using a laser power of 45 µW, which, based on prior experiments, does not indicate significant heating (see section 4.6).

Furthermore, reproducing the observed effect in figure 4.6a through simulations becomes challenging at such low laser power levels. Here a saturation in the vicinity of 1 to $2I_{\text{sat}}$ is necessary, the simulation in figure 4.5a has also been performed with $2I_{\text{sat}}$. Measuring the saturation curve for micrometer sized diamonds however did not yield any result, thus the true saturation intensity is unknown. Further as the micrometer sized diamond particle is larger than the focused laser spot size, the laser intensity encountered

by the NV centers inside this diamond particle will be highly non uniform.

To conclude, throughout this thesis, I have used this result for other simulations, while it has to be stated that the measured value is not fully understood. The greatest impact such a short lifetime has on the simulations, is that it lowers the spin dependent PL contrast. The individual decay rates are then derived from the assumption that the decay into the `3A2` ($m_s = 0$) spin state is twice as likely as the decay into the $m_s = \pm 1$ manifold combined [15] leading to $\gamma_{40} = 22\,\text{MHz}$ and $\gamma_{41} = 11\,\text{MHz}$.

4.5. Ground State Spin Relaxation Time

In sections 4.2 to 4.4, the coupling strengths and relaxation rates for transitions between excited states of the NV center were measured. This section focuses on further investigating the spin properties of the `3A2` ground state.

A direct measurement of the longitudinal spin relaxation time (T1) of the `3A2` ground state ($m_s = 0 \rightarrow m_s = 0/\pm 1$) is presented here. The measurement follows a similar methodology to the spin readout described in section 3.2.1, but employs a pump-pump-probe scheme instead of the pump-probe scheme. This approach is necessitated by technical constraints, as rapid sequences are prerecorded into the Sinara-Kasli RAM for more robust experiment parameterization. This RAM is limited in size and can approximately only hold up to a few thousand sequence repetitions. Experimentally, this means that the $\sim 10^5$ sequence repetitions making up each data point are divided into many batches which are played back sequentially. The time between the playback of two sequential batches is then not the same compared to the time between repetitions of the same sequence within the same batch. Thus, an extra pump pulse is included to ensure the system is always in the same initial state. This scheme is also schematically drawn in figure 4.7a.

The spin readout is performed by computing the visibility from the two leading edges of the second pump and the probe pulses. The experiment was conducted at $2\,\text{mW} \approx \frac{1}{2} I_{\text{sat}}$ (section 4.3) on ND10. As the visibility is calculated by comparing the initial PL of the probe pulse to that of the pump pulse (see equation (3.1)), a saturated exponential rise in this visibility is observed as the polarization of the `3A2` spin reduces due to spin relaxation, increasing the visibility. Note that in figure 4.7b the y axis is inverted. By fitting a single exp. function to this data (red line), a time constant $\text{T1} = 280(70)\,\mu\text{s}$ for this spin relaxation time is obtained.

This value is shorter than what has been reported for other commercial HTHP Nanodiamonds containing ensembles of NV centers, e.g. 3.6 ms [46].

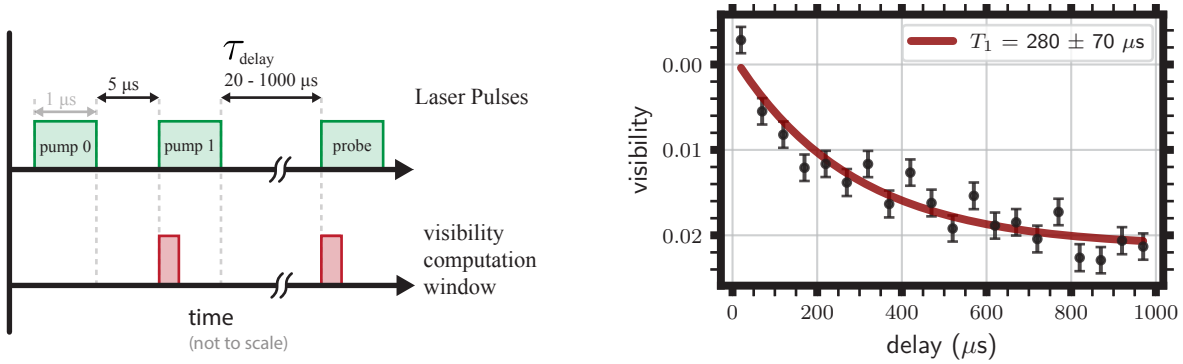

(a) Sequence Sketch (b) Experiment

Figure 4.7.: **Spin Relaxation Time**
The visibility (equation (3.1)) of the probe with respect to the pump 1 pulse in a pump-pump-probe scheme is measured as a function of the delay time in-between the probe and pump 1 pulse. The measurement sequence is sketched out in (a). The measurement signal is given by the visibility (equation (3.1)); note the inverted y-axis. A single exponential fit yields the longitudinal spin relaxation time, $T_1 = 280 \pm 70\,\mu s$.

4.6. Optically Detected Magnetic Resonance Spectroscopy Measurements

While the previous experimental results relied solely on a single laser driving all of the 3A2 to 3E transitions, in the next sections an additional driving between the $m_s = 0$ and $m_s = +1$ or $m_s = -1$ sub-levels of the 3A2 state is added. This driving is delivered via the resonant microwave magnetic field coil (MW), section 3.1.4. In this section, the use of ODMR is also showcased (section 3.2.2).

4.6.1. Measuring Temperature and Laser Induced Heating

In section 2.2.2 an analytical description was shown how to calculate the ZFS (D) of the 3A2 ground state as a function of temperature. Here the ZFS shift is measured allowing the resulting temperature to be calculated. This firstly quantifies relative heating effects, but also allows to extract an absolute temperature via the use of the phonon mode energies and weights, as discussed in section 2.2.2. To do so we invert equation (2.5) by numerically solving the following equation

$$D(T) - D_{\text{meas}} = 0. \tag{4.11}$$

Now turning to experiment, in Figure 4.8 the ODMR spectrum of a micrometer sized diamond is measured for three different illumination laser powers: 0.045, 3 and 20 mW. The data is fitted with a double lorenzian fit function (solid line) from which the zero field splitting parameter, D, is extracted as the mean of the two resonance frequencies obtained through the fit. This value is then used to calculate the absolute temperature of the diamond crystal according to equation (4.11).

In this measurement the three ODMR spectra show a double resonance structure that with increasing laser power clearly shifts towards lower MW frequencies. This is expected to be the result of the focused laser spot, heating up the diamond or also the surrounding substrate. The double resonance is likely to a stray magnetic field of approximately 1.5 G within the setup, lifting the between the two spin projections $m_s = 1$ and $m_s = -1$ by approximately 8.4 MHz in the case of 3 and 20 mW laser power. A second observation of figure 4.8 is, that the relative magnitude of the ODMR dip decreases with increasing driving power. This is expected as here, the steady state equilibrium here between the laser polarizing into the $m_s = 0$ projection vs. a resonant MW mixing these states again, is measured, leading to a dip in the PL (see also section 3.2.2). A much greater laser driving will re-polarize the state faster than the MW could mix them. This will reduce the observed contrast at resonance.

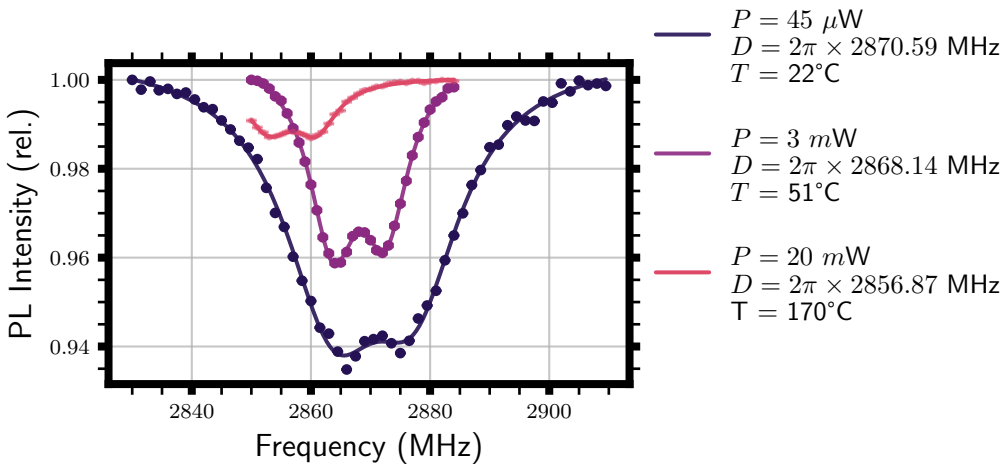

Figure 4.8.: **Laser Heating of a single Diamond Particle (Microdiamond)** The ODMR spectrum of a microdiamond, containing many NV centers is recorded for different laser illumination powers. Here the focused laser spot is smaller then the size of the diamond particle which is $\approx 15\,\mu$m. The solid line in each measurement corresponds to a double lorenzian fit function. This double lorenzian function is derived by adding two individual lorenzian (equation (4.12)). For each measurement, the ZFS is then given as the mean of the two resonances obtained from the fit. With this value, the absolute temperature of the diamond crystal is computed from equation (4.11), using the parameters shown in table 2.1.

4.6.2. Determining the Diamond Particle's Orientation with respect to an External Magnetic Field

As described in section 2.2, a mono-crystalline diamond allows for four different orientation of the NV center (figure 2.2). A global magnetic field will lift this degeneracy of the different NV center orientations via the Zeeman effect (equation (2.2)). However, when working with diamond particles, generally one does not know the orientation of the diamond lattice. Nevertheless if all eight frequency shifts associated with the four orientations of the $m_s = \pm 1$ spin vector are measured then, this orientation can be derived.

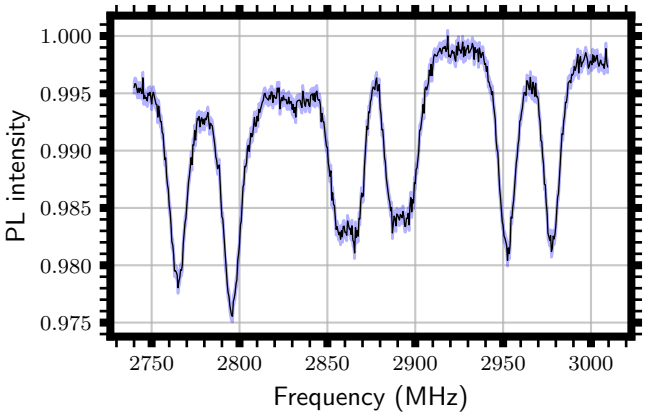

Figure 4.9.: **ODMR Spectroscopy of a Microdiamond under an External Magnetic Field**
The relative PL is plotted while the frequency of the MW coil is scanned. A permanent magnet is used to resolve the degeneracy of the different NV axes. The shaded blue region represents the shot noise error. The outer four dips correspond to the spin flip transitions of individual NV center axes, where as the two inner dips are due to four transitions where the individual transitions are not fully resolved. Here, a double lorenzian fit is used to extract the resonance frequency of the individual transitions.

Figure 4.9 shows how under a static magnetic field a degenerate ensemble of NV centers will split in up to eight lorenzian peaks. There these frequency shifts are extracted by fitting individual lorenzian functions, each defined as

$$f(\omega) = a + \frac{2A\Gamma_l}{\pi(4(\omega - \omega_0)^2 + \Gamma_l^2)} \tag{4.12}$$

where A, a are the amplitude and offset respectively, ω is the MW frequency and ω_0 the resonance frequency and Γ_l the full-width-half-maximum (FWHM) of the observed dip in PL. The resonance frequencies obtained from this are shown in table 4.2. Using these values and the corresponding Zeeman splittings, we can now follow the derivation shown in section A.2 and calculate the DC Magnetic field vector with respect to the NV

Index	**Frequency** ω_0 in [MHz/2π]	**FWHM Width** Γ_l in [MHz/2π]
1	2765.09(5)	14.4(8)
2	2795.57(5)	13.7(5)
3	2856	13.1(5)
4	2866	13.1(5)
5	2887	14.0(5)
6	2897	14.0(5)
7	2952.48(5)	13.3(4)
8	2977.65(5)	11.8(3)

Table 4.2.: **Fit Results to ODMR spectroscopy presented in Figure 4.9**
By individually fitting four single and two double lorenzian curves (equation (4.12)) to the spectrum shown in figure 4.9 the resonance frequency ω_0 as well as the full width half maximum (FWHM) of the peaks Γ are determined.

centers crystal lattice. Here, we use the following convention: The two outermost dips in figure 4.9 are due to the interaction of the constant magnetic field with the NV center whose axis is most parallel to the magnetic field vector. The second outermost dips are then due to the NV center oriented along the axes which has the second closest angle to $\vec{B}$, and so on. By this logic a splitting vector $\Delta\vec{\omega}$, using the frequency differences, is calculated as

$$\Delta\vec{\omega} = \begin{pmatrix} \omega_8 - \omega_1 \\ \omega_7 - \omega_2 \\ \omega_6 - \omega_3 \\ \omega_5 - \omega_4 \end{pmatrix} \tag{4.13}$$

where ω_i is the resonance frequency of index i from table 4.2. We now choose that the z-axis corresponds to the diamond lattice vector that has the smallest angle with $\vec{B}$. We label this lattice vector $\hat{n}_1$. Following the derivation shown in section A.2, the magnitude $\vec{B}$ is then given by:

$$B_0 = \frac{\sqrt{3}\hbar}{8\mu_\mathrm{B}} \|\Delta\vec{\omega}\| \tag{4.14}$$

and the angle θ of $\vec{B}$ with respect to $\hat{n}_1 = \hat{e}_z$ is given by

$$\theta_B = \arccos\left(\frac{2\Delta\omega_1}{\sqrt{3}\|\Delta\vec{\omega}\|}\right) \tag{4.15}$$

where $\Delta\omega_1$ is the upper most entry in $\Delta\vec{\omega}$. For the values of table 4.2 we obtain $B_0 = 4.15\,\mathrm{mT}$ and $\theta = 23.8°$.

4.6.3. Optically Detected Magnetic Resonance Spectroscopy with Nanodiamonds

The measurements presented in section 4.6.2 and the measurement shown in figure 4.9 were performed on a microdiamond ($\approx 15\,\mu m$ size). In this section a similar feature of lifting the degeneracy of different NV orientations is attempted using a nanodiamond. This will be necessary for selecting a single NV orientation to which we want to couple to coherently.

Figure 4.10 shows two different kind of ODMR spectroscopy measurements performed on ND10, with the same static magnetic field applied to lift the degeneracy of the different NV orientations. The first one, figure 4.10a, shows an ODMR measurement at greatly decreased laser power ($300\,\mu W$) similar to the ODMR spectra obtained in section 4.6.1. However, obtaining a clean ODMR signal proved to be difficult due to strong fluctuations in the laser intensity on long timescales not explainable by NV dynamics. Nevertheless, a MW-Frequency of 2850 MHz from this experiment was chosen as the static MW frequency for the following Rabi oscillation measurement (section 4.7).

After measuring a π time in figure 4.11 of approximately 250 ns, which is detailed in the following (section 4.7), a second kind of ODMR measurement was attempted. Instead of reducing the laser power greatly and observing the steady state PL as a function of MW frequency, here a pulsed scheme was used. The layout of this scheme is drawn in figure 4.10c. Here a MW Pulse at a fixed length, which is chosen to be equal to the π-time, and is played in-between the second pump and first probe pulse in a pump-pump-probe sequence. The measurement consists of recording the visibility while the frequency of this π-pulse is swept (figure 4.10b). Here two major broadened peaks are observable. This is likely due to the degenerate NV center orientations which could not be split far enough with the applied static magnetic field.

Another observation is that ODMR measurement at the low power in (a) shows the expected zero field splitting of ≈ 2870 MHz. In contrast, the pulsed ODMR measurement which was performed at much higher laser power, which shows a shifted zero field splitting to 2867.5 MHz. Using equation (2.5), this would correspond to absolute temperatures of 30 and 63 °C respectively.

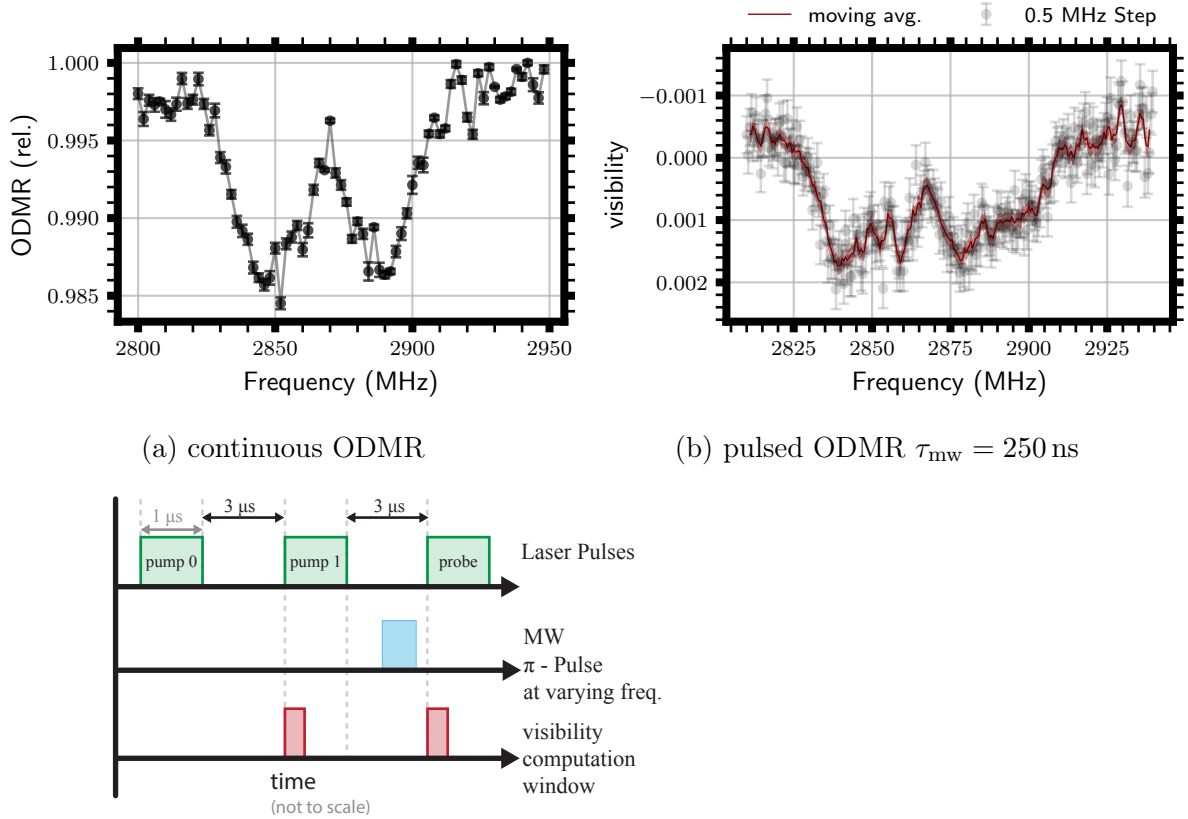

(a) continuous ODMR

(b) pulsed ODMR $\tau_{\mathrm{mw}} = 250\,\mathrm{ns}$

(c) Pulsed ODMR Scheme

Figure 4.10.: **Steady State and Pulsed ODMR with ND10**
(a) shows the ODMR spectrum obtained from the nanodiamond ND10. A static magnetic field is applied to split the degeneracy of the different NV center orientations. Here only a double resonance feature was obtainable with a frequency splitting of approx. 55 MHz, which would point toward a magnetic field of approx. 10 G. In (b) a pulsed ODMR measurement is shown for comparison. The sequence of this measurement is explained in (c). In addition a moving average filter (red-line) with a window size of 2.5 MHz is applied. The light red shaded area indicates the standard error of this moving average.

4.7. Electronic Spin Coherence of the Nitrogen-Vacancy Center

Let us finally turn to the coherent spin properties of the NV center. In solid state spin systems, often three relevant timescales are used: T1, T2 and T2*. As already discussed above, T1 is the characteristic time at which the NV centers spin flips, i.e. the longitudinal relaxation time (along the quantization axis). T2* refers to the inhomogeneous spin dephasing time, which is the characteristic timescale over which fringe contrast in a Ramsey-interferometer-type experiment would disappear. These inhomogeneities can often be suppressed by dynamical decoupling schemes such as a Hahn-Echo or more complex sequences, yielding the best achievable coherence time of the system, denoted as T2. For NV centers at room temperature the highest achieved T2 times are on the order of 2.4 ms for single NV centers in isotopically purified, CVD-grown bulk diamond [16]. For nanodiamonds, surface effects lead to increased decoherence with the highest achieved T2 values on the order of 700 µs [47, 48].

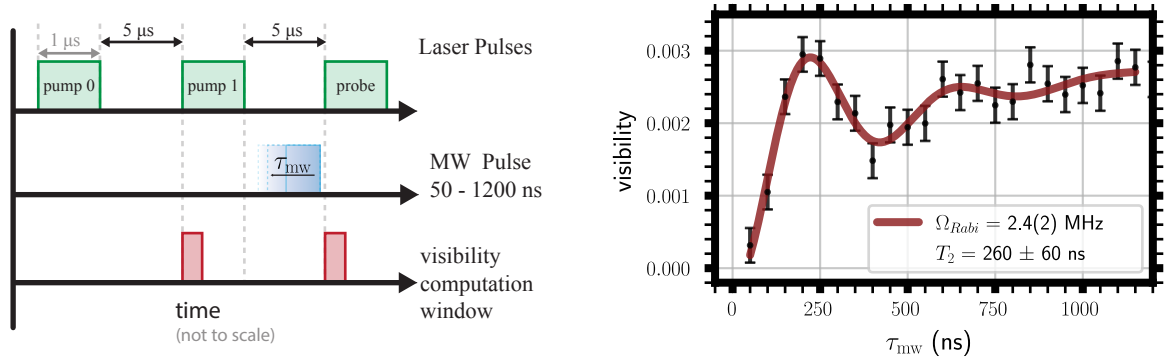

(a) Measurement sequence

(b) Rabi oscillations

Figure 4.11.: **Coherent Rabi Oscillations of NV Center Ensembles in ND10** In (a) the pump-pump-probe scheme is sketched. A fixed 5 µs delay is set between the second pump and probe pulse. Between the pump1 and probe pulse, a MW pulse (2850 MHz) with varying length is scheduled. The timing of the pulse is such, that the time between MW pulse end and probe pulse start remains constant. In (b), the visibility, calculated from the initial PL of the pump1 and probe pulses using equation (3.1), is plotted as a function of the MW pulse length. An exponentially dampened sine function is fit to the data (red)

In this thesis, a T2 time for a non-isotopically purified, HTHP-produced, NV-ensemble nanodiamond of 260 ± 60 ns is reported. In figure 4.11 collective Rabi oscillations, between two spin states of the `3A2` ground state, are observed by varying the time τ_{mw} of a resonant mw pulse applied between the two laser probe-pulses of a pump-pump-probe measurement. Figure 4.11a shows a sketch of each single sequence, which is rapidly repeated for a varying MW pulse length. In figure 4.11b the resulting visibility,

computed over many repetitions of the same sequence, is plotted. The red line represents a fit to an exponentially damped sine function, which is used to estimate the oscillation frequency of 2.4(2) MHz as well as the exponential damping constant (T2) of 260 ns. This measured T2 time is relatively short compared to T2 times on the order of single digit μs that have been achieved in HTHP, NV center ensemble, nanodiamond systems [46, 49]. It should be noted that the measurement in figure 4.11b was the first successful observation of Rabi oscillations on this setup, and no further optimization has been implemented so far. Further, I refer to the measurement presented in figure 4.10b in which no clear splitting of the degenerate NV center orientations was achieved. Thus it is likely that at the chosen MW frequency of 2850 MHz, an inhomogeneous coupling to multiple NV center ensembles smeared out the observed coherence.

5. Discussion and Outlook

This thesis marks the first work on NV centers within our research group, and also within Innsbruck. This meant that all of the experimental setup had to be constructed from the beginning. Many of the measurements presented in chapter 4 have not yet had the benefit of optimization. In fact all of the spin properties measured with ND10 became only possible towards the end of my work in the lab. In this chapter I reflect on some of these parts.

5.1. Experimental Setup

In section 3.1.1 the build up of a confocal microscope is detailed. In the future, this confocal microscope setup is intended to be used as a test setup for Nanodiamond Properties. The aim of the research is doing these experiments with levitated diamond particles in vacuum.

Visibility Based Spin Readout A significant experimental achievement of this thesis is the development of visibility-based spin readout, which facilitated the measurement of spin properties such as coherent Rabi oscillations (section 4.7) and spin relaxation rates over longer timescales (section 4.5).

The primary motivation for adopting visibility as the spin readout method stemmed from the observed PL from nanometer-sized diamond particles, which exhibited substantial drifts compared to the spin-dependent PL differences. These PL drifts had previously hindered the aforementioned measurements.

The advantage of using visibility, as defined in equation (3.1), lies in its insensitivity to linear PL drifts, such as fluctuations in laser intensity over timescales longer than a single sequence (approximately 10 µs). Unlike absolute PL differences, visibility is only weakly affected by constant offsets, making it a more robust method for spin readout.

Software Setup A significant portion of the time spent building the setup was dedicated to establishing the software infrastructure. One major effort involved writing sequences that utilized the TTL input of the Sinara for time tagging. Integrating this functionality into a sequence capable of collecting many photons over multiple repetitions proved challenging, as the TTL input's FFIO buffer could only store 74 int64 numbers before overflowing. This required developing an efficient method to execute as many sequences as quickly as possible while scheduling buffer readouts effectively.

Ultimately, this approach was abandoned when a dedicated time tagger became available, enabling the continuous recording of numerous sequences without such constraints.

However, an important outcome of this effort was the creation of parameterized experimental scripts that stored their parameter values as metadata directly within the experiment data file. Here the HDF5 data format was implemented as it is widely used in the scientific community. This led to the development of a data-saving software module, which has since become a fundamental piece of the the data-saving infrastructure used across our laboratory.

5.2. NV center Properties in Diamond Particles

Determining the Radiative Decay Rates In section 4.2 the fluorescence lifetime of the NV centers PL is measured. This process is described by four different parameters which can not all be resolved through fitting to the observed data. Thus literature values were consulted. I am however only aware of individual rate measurements on single NV centers housed inside comparatively large diamond particles and not of any rigorous studies of decay rates in nanodiamonds. It is reported that the observed long fluorescence lifetime is due to the suppression of radiative decay while making the assumption that the non-radiative rate remains unchanged (section 2.2.3). In the current setup, a direct measurement of the non radiative decays is not possible. This is due to the fact that the laser's 10 ns rise(fall)-time hinders closer study as the $m_s = \pm 1$ manifold of 3E decays on the same timescale of a single optical cycle. With a faster pulsed laser, a similar measurement as shown in [21] could be performed that can resolve the different dynamics of the two spin projections which would also enable determining the polarization of the excited states manifold.

One other consideration that should be noted here is that the contribution of the NV^0 was not separately added here. While in section 4.1 a significant NV^0 contribution is observed the extend of this is not known. The product page of the nanodiamonds manufacturer (Adamas) also does not specify this value. However for the smaller sized Nanodiamonds in the 10 to 13 nm size range, they estimate a 60 % NV^0 and 40 % NV^- ratio. Such a large NV^0 contribution would almost certainly influence the measurement performed there.

Singlet State Lifetime In section 4.4 an attempt was made at measuring the lifetime of the singlet state manifold for a microdiamond particle hosting a high density of NV centers. However, the measured values are not fully understood. This lifetime (30 ns) is significantly shorter than reported values in literature (approx. 100 ns). We, however, emphasize that the available literature values have been measured with isolated NV centers. Understanding the value measured within this thesis will be the effort of future investigations.

Spin Relaxation and Dephasing Rate, T1 and T2 In sections 4.5 and 4.7 the spin relaxation time, (T1) and dephasing time (T2) of the 3A2 ground state were determined to be 280(70) µs and 260(60) ns respectively. For comparison, Jin et al. [46], which use,

approximately 750 nm large nanodiamonds supplied by the same vendor, measure a T1 and T2 time for of 2.34 ms and 2.98 µs respectively.

Compared to these findings, the T1 and T2 values in this thesis are lower. However, as here only one nanodiamond (ND10) was measured, more statistics will have to be acquired by measuring different nanodiamonds to properly conclude on these properties.

Further, the observed T2 time may also be subject to dephasing due to simultaneous coupling of spin states in different NV center orientations. For future measurements it is recommended to first realize a dedicated splitting and to address a single class of NV center orientations only.

Temperature Effects In section 4.6.1, the zero field splittings D in micrometer sized diamond particles were measured at different green laser illumination powers. From equation (4.11) an absolute temperature of the host diamond crystal is calculated. Qualitatively these absolute temperatures seem reasonable. During this measurement the temperature of the diamond could not be independently measured however the lab temperature at the time of this measurement (measured on a different setup) was between 22 and 23 °C, consistent with the temperature that was extracted from the measurement.

In a future experiment it would be interesting to independently verify this temperature dependence for nanodiamonds. As laser heating has been demonstrated here, it could further be tested if laser refrigeration of diamond crystals is observable by strongly driving the anti stokes sideband of the $^3A_2 \rightarrow {}^3E$ which according to theory might be possible [50].

A. Appendix

A.1. Saturation Intensity

The magnitude of collected Photoluminescence PL(I) from a driven two level system as a function of resonant laser intensity I is empirically given as

$$\mathrm{PL}(I) = \mathrm{PL}_{\max}\frac{I}{I + I_{\mathrm{sat}}} \tag{A.1}$$

where $\mathrm{PL}_{\max}$ corresponds to the maximum PL at infinite driving power and I_{sat} the saturation intensity.

In the following this dependency shall be derived for the case of a two level system where in addition to the optical decay $\Gamma = 1/T_1$ an additional dephasing of the excited state $\xi = 1/T_2$ is included.

The interaction picture Hamiltonian of the system in the rotating frame is given by

$$V = \Delta \left|e\right\rangle \left\langle e\right| - \frac{\Omega}{2}(\left|e\right\rangle \left\langle g\right| + \left|g\right\rangle \left\langle e\right|) \tag{A.2}$$

where Δ is the detuning of the laser frequency ω_L with respect to the energy splitting ω_0 and Ω the rabi frequency of the driving. We consider the following master equation in Lindblad form ($\hbar = 1$)

$$\dot{\rho} = -i[V, \rho] + \sum_k \left(L_k \rho L_k^\dagger - \frac{1}{2} L_k^\dagger L_k \rho - \frac{1}{2} \rho L_k^\dagger L_k \right) \tag{A.3}$$

with the collapse operators L_k

$$\begin{aligned} L_1 &= \sqrt{\Gamma}|g\rangle\langle e| && \text{decay} |e\rangle \to |g\rangle \text{ at rate } \Gamma \\ L_2 &= \sqrt{\xi}|e\rangle\langle e| && \text{dephasing of } |e\rangle \text{ at rate } \xi. \end{aligned}$$

This leads to the following Bloch equations

$$\dot{\rho}_{ee} = -\Gamma \rho_{ee} - i\frac{\Omega}{2}(\rho_{eg} - \rho_{ge}) \tag{A.4}$$

$$\dot{\rho}_{eg} = -(\xi/2 + \Gamma/2 + i\Delta)\rho_{eg} - i\frac{\Omega}{2}(\rho_{ee} - \rho_{gg}) \tag{A.5}$$

$$1 = \rho_{ee} + \rho_{gg} \tag{A.6}$$

$$\rho_{eg} = \rho_{ge}^* \tag{A.7}$$

ρ_{ij} denotes $\langle i|\,\rho\,|j\rangle$.

We are interested in the steady state solution when

$$\dot{\rho}_{ee} = \dot{\rho}_{gg} = \dot{\rho}_{eg} = 0.$$

From equation (A.4) to equation (A.7) using $\rho_{eg} = x + iy$ we then get

$$0 = -\Gamma\rho_{ee} + \Omega y \tag{A.8}$$

$$0 = -\frac{1}{2}(\xi + \Gamma + 2i\Delta)(x + iy) - i\frac{\Omega}{2}(2\rho_{ee} - 1). \tag{A.9}$$

Equation (A.9) can be split into real and Imaginary part:

$$\text{Re}: \qquad 0 = -\frac{1}{2}(\xi + \Gamma)x + \Delta y \tag{A.10}$$

$$y = \frac{\xi + \Gamma}{2\Delta}x \tag{A.11}$$

$$\text{Im}: \qquad 0 = -\Delta x - \frac{y}{2}(\xi + \Gamma) - \frac{\Omega}{2}(2\rho_{ee} - 1). \tag{A.12}$$

Now from equation (A.8) and equation (A.11) we get

$$0 = -\Gamma\rho_{ee} + \frac{\Omega}{2}\frac{\xi + \Gamma}{\Delta}x$$

$$x = \frac{2\Delta\Gamma\rho_{ee}}{\Omega(\xi + \Gamma)}.$$

Now substituting x and solving for ρ_{ee} yields

$$0 = -x\frac{4\Delta^2 + (\xi + \Gamma)^2}{4\Delta} - \frac{\Omega}{2}\rho_{ee} + \frac{\Omega}{2}$$

$$0 = -\frac{2\Delta\Gamma\rho_{ee}}{\Omega(\xi + \Gamma)}\frac{4\Delta^2 + (\xi + \Gamma)^2}{4\Delta} - \Omega\rho_{ee} + \frac{\Omega}{2}$$

$$0 = -\rho_{ee}\frac{2\Delta^2\Gamma + \frac{1}{4}\Gamma(\xi + \Gamma)^2}{\Omega(\xi + \Gamma)} - \Omega\rho_{ee} + \frac{\Omega}{2}$$

which can now be rewritten as

$$\rho_{ee} = \frac{\Omega^2}{4\Delta^2(\frac{\Gamma}{\xi+\Gamma}) + \Gamma(\xi + \Gamma) + 2\Omega^2} \tag{A.13}$$

or in the case of resonant driving ($\Delta = 0$) be reduced to

$$\rho_{ee} = \frac{1}{2}\frac{\Omega^2}{\Omega^2 + \frac{\Gamma(\Gamma+\xi)}{2}}. \tag{A.14}$$

Because the rate at which spontaneous decay can happen is proportional to the excited state population ρ_{ee} only, and $I \sim \Omega^2$ we can now relate equation (A.14) to equation (A.1) and identify the saturation intensity $I_{\text{sat}} \sim \Omega^2_{\text{sat}}$ as

$$I_{\text{sat}} = \frac{\Gamma(\Gamma + \xi)}{2}. \tag{A.15}$$

A.2. Orientation of the DC Magnetic Field with respect to the Diamond Crystal Orientation

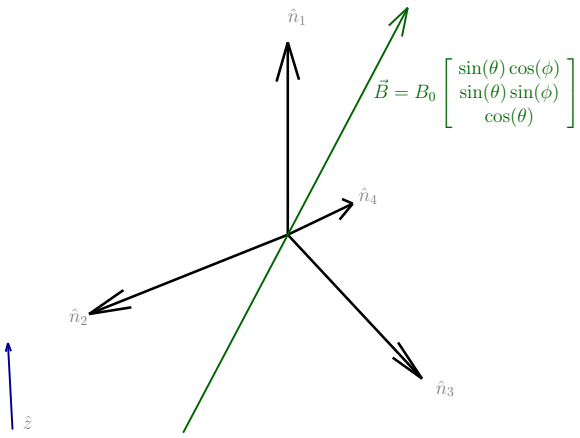

Figure A.1.: **Basis Vectors of the Four Possible NV Center Orientations** For this calculation we choose a coordinate system such that the z-axis is aligned to the first crystallographic [1, 1, 1] direction which is denoted by $\hat{n}_1$. The green vector represents an arbitrary static magnetic field at some angle with respect to the diamond in spherical coordinates with θ the polar- and ϕ the azimuthal angle.

We can write the basis vectors in the polar coordinate system by using the angle between two lattice vectors given as $\theta_D = \arccos(-1/3) \approx 109.5°$ and the azimuthal angle of the other three lattice vectors which have a three fold rotational symmetry. For this, we choose $\phi_{\hat{n}_2} = 0$ thus $\phi_{\hat{n}_{3,4}} = [\frac{2}{3}\pi, \frac{4}{3}\pi]$. In spherical coordinates where $\hat{n}_i = [r_i, \theta_i, \phi_i]$ the vectors are therefore defined as

$$\begin{aligned} \hat{n}_1 &= [1, 0, 0] \\ \hat{n}_2 &= [1, \theta_D, 0] \\ \hat{n}_3 &= [1, \theta_D, \frac{2}{3}\pi] \\ \hat{n}_4 &= [1, \theta_D, \frac{4}{3}\pi] \end{aligned} \tag{A.16}$$

or in Cartesian coordinates as

$$\begin{aligned}
\hat{n}_1 &= \begin{pmatrix} 0 \\ 0 \\ 1 \end{pmatrix} \\
\hat{n}_2 &= \begin{pmatrix} \sin(\theta_D) \\ 0 \\ \cos(\theta_D) \end{pmatrix} = \frac{1}{3}\begin{pmatrix} 2\sqrt{2} \\ 0 \\ -1 \end{pmatrix} \\
\hat{n}_3 &= \begin{pmatrix} \sin(\theta_D)\cos(\phi_{\hat{n}_3}) \\ \sin(\theta_D)\sin(\phi_{\hat{n}_3}) \\ \cos(\theta_D) \end{pmatrix} = \frac{1}{3}\begin{pmatrix} -\sqrt{2} \\ \sqrt{6} \\ -1 \end{pmatrix} \\
\hat{n}_4 &= \begin{pmatrix} \sin(\theta_D)\cos(\phi_{\hat{n}_4}) \\ \sin(\theta_D)\sin(\phi_{\hat{n}_4}) \\ \cos(\theta_D) \end{pmatrix} = -\frac{1}{3}\begin{pmatrix} \sqrt{2} \\ \sqrt{6} \\ 1 \end{pmatrix}
\end{aligned} . \tag{A.17}$$

Now from equation (2.3) we get two values for each NV orientation. If we obtain a spectrum with eight resolvable peaks, such as in figure 4.9 than we can label these peaks from left to right with the corresponding lattice side $[\hat{n}_1', \hat{n}_2', \hat{n}_3', \hat{n}_4', \hat{n}_4', \hat{n}_3', \hat{n}_2', \hat{n}_1']$. Where $\hat{n}_1'$ is the lattice vector most parallel to the magnetic field, and $\hat{n}_4'$ the most orthogonal thus responsible for the lowest energy shift. The notation $\hat{n}_i'$ is used to denote a currently unknown permutation of the vectors $\{\hat{n}_i\}$. Now from this ordering we can calculate the observed frequency splittings $\Delta\omega_i$ defined as

$$\Delta\omega_i = \frac{4\mu_\mathrm{B}}{\hbar} B_0 \left| \begin{pmatrix} \sin(\theta_B)\cos(\phi_B) \\ \sin(\theta_B)\sin(\phi_B) \\ \cos(\theta_B) \end{pmatrix} \cdot \hat{n}_i' \right| . \tag{A.18}$$

Here $\Delta\omega_1$ corresponds to the splitting obtained by taking difference in frequency of the outer most dips, $\Delta\omega_2$ the second to outermost,.. and finally $\Delta\omega_4$ the inner most dips. Thus $\Delta\omega_1 > \Delta\omega_2 > \Delta\omega_3 > \Delta\omega_4$. By calculating the norm $\|\vec{\Delta\omega}\|$ we obtain the magnitude of the magnetic field B_0 as

$$B_0 = \frac{\sqrt{3}\hbar}{8\mu_\mathrm{B}} \|\vec{\Delta\omega}\|. \tag{A.19}$$

This can be shown considering an arbitrary vector $\vec{a}$ and and taking the norm of the matrix product $\vec{a}\,(\hat{n}_1, \hat{n}_2, \hat{n}_3, \hat{n}_4)$

$$\|\vec{a}\,(\hat{n}_1, \hat{n}_2, \hat{n}_3, \hat{n}_4)\,\| = \sqrt{(\vec{a}\cdot\hat{n}_1)^2 + (\vec{a}\cdot\hat{n}_2)^2 + (\vec{a}\cdot\hat{n}_3)^2 + (\vec{a}\cdot\hat{n}_4)^2} = \frac{2}{\sqrt{3}}\|\vec{a}\|$$

Moving forward, will choose $\hat{n}_1' = \hat{n}_1$ essentially i.e. choosing that in our arbitrary coordinate system, $\hat{n}_1$ will be the vector that is closest to $\vec{B}$. There we can drop the norm,$|\cdot|$, from equation (A.18) as this angle by definition is now $< 109.5/2$. Then the polar angle θ_B of magnetic field with respect to $\hat{n}_1$ is given by

$$\theta_B = \arccos\left(\frac{2\Delta\omega_1}{\sqrt{3}\|\vec{\Delta\omega}\|}\right). \tag{A.20}$$

References

1. Hensen, B. *et al.* Loophole-Free Bell Inequality Violation Using Electron Spins Separated by 1.3 Kilometres. *Nature* **526.** doi:10.1038/nature15759 (2015).
2. Bell, J. S. On the Einstein Podolsky Rosen Paradox. *Physics Physique Fizika* **1.** doi:10.1103/PhysicsPhysiqueFizika.1.195 (1964).
3. Freedman, S. J. Experimental Test of Local Hidden-Variable Theories. *Phys. Rev. Lett.* **28.** doi:10.1103/PhysRevLett.28.938 (1972).
4. Aspect, A. Experimental Test of Bell's Inequalities Using Time-Varying Analyzers. *Phys. Rev. Lett.* **49.** doi:10.1103/PhysRevLett.49.1804 (1982).
5. Weihs, G. Violation of Bell's Inequality under Strict Einstein Locality Conditions. *Phys. Rev. Lett.* **81.** doi:10.1103/PhysRevLett.81.5039 (1998).
6. Doherty, M. W., Manson, N. B., Delaney, P., Jelezko, F., Wrachtrup, J. & Hollenberg, L. C. L. The Nitrogen-Vacancy Colour Centre in Diamond. *Physics Reports* **528.** doi:10.1016/j.physrep.2013.02.001 (2013).
7. Hopper, D. A., Shulevitz, H. J. & Bassett, L. C. Spin Readout Techniques of the Nitrogen-Vacancy Center in Diamond. *Micromachines* **9.** doi:10.3390/mi9090437 (9 2018).
8. Schirhagl, R., Chang, K., Loretz, M. & Degen, C. L. Nitrogen-Vacancy Centers in Diamond: Nanoscale Sensors for Physics and Biology. *Annu. Rev. Phys. Chem.* **65.** doi:10.1146/annurev-physchem-040513-103659 (2014).
9. Marshman, R. J., Mazumdar, A., Folman, R. & Bose, S. Constructing Nano-Object Quantum Superpositions with a Stern-Gerlach Interferometer. *Phys. Rev. Res.* **4.** doi:10.1103/PhysRevResearch.4.023087 (2022).
10. Aspelmeyer, M. in *From Quantum to Classical: Essays in Honour of H.-Dieter Zeh* (Springer International Publishing, 2022). doi:10.1007/978-3-030-88781-0_5.
11. Gonzalez-Ballestero, C., Aspelmeyer, M., Novotny, L., Quidant, R. & Romero-Isart, O. Levitodynamics: Levitation and Control of Microscopic Objects in Vacuum. *Science* **374.** doi:10.1126/science.abg3027 (2021).
12. Deng, B., Zhang, R. Q. & Shi, X. Q. New Insight into the Spin-Conserving Excitation of the Negatively Charged Nitrogen-Vacancy Center in Diamond. *Sci Rep* **4.** doi:10.1038/srep05144 (2014).
13. Gali, Á. Ab Initio Theory of the Nitrogen-Vacancy Center in Diamond. *Nanophotonics* **8.** doi:10.1515/nanoph-2019-0154 (2019).

14. Ernst, S., Scheidegger, P. J., Diesch, S., Lorenzelli, L. & Degen, C. L. Temperature Dependence of Photoluminescence Intensity and Spin Contrast in Nitrogen-Vacancy Centers. *Phys. Rev. Lett.* **131.** doi:10.1103/PhysRevLett.131.086903 (2023).

15. Happacher, J., Bocquel, J., Dinani, H. T., Tschudin, M. A., Reiser, P., Broadway, D. A., Maze, J. R. & Maletinsky, P. Temperature-Dependent Photophysics of Single NV Centers in Diamond. *Phys. Rev. Lett.* **131.** doi:10.1103/PhysRevLett.131.086904 (2023).

16. Herbschleb, E. D. *et al.* Ultra-Long Coherence Times amongst Room-Temperature Solid-State Spins. *Nat Commun* **10.** doi:10.1038/s41467-019-11776-8 (2019).

17. Pham, L. M., Bar-Gill, N., Le Sage, D., Belthangady, C., Stacey, A., Markham, M., Twitchen, D. J., Lukin, M. D. & Walsworth, R. L. Enhanced Metrology Using Preferential Orientation of Nitrogen-Vacancy Centers in Diamond. *Phys. Rev. B* **86.** doi:10.1103/PhysRevB.86.121202 (2012).

18. Ivády, V., Simon, T., Maze, J. R., Abrikosov, I. A. & Gali, A. Pressure and Temperature Dependence of the Zero-Field Splitting in the Ground State of NV Centers in Diamond: A First-Principles Study. *Phys. Rev. B* **90.** doi:10.1103/PhysRevB.90.235205 (2014).

19. Tang, H., Barr, A. R., Wang, G., Cappellaro, P. & Li, J. First-Principles Calculation of the Temperature-Dependent Transition Energies in Spin Defects. *J. Phys. Chem. Lett.* **14.** doi:10.1021/acs.jpclett.3c00314 (2023).

20. Cambria, M. C., Thiering, G., Norambuena, A., Dinani, H. T., Gardill, A., Kemeny, I., Lordi, V., Gali, Á., Maze, J. R. & Kolkowitz, S. Physically Motivated Analytical Expression for the Temperature Dependence of the Zero-Field Splitting of the Nitrogen-Vacancy Center in Diamond. *Phys. Rev. B* **108.** doi:10.1103/PhysRevB.108.L180102 (2023).

21. Robledo, L., Bernien, H., Sar, T. V. D. & Hanson, R. Spin Dynamics in the Optical Cycle of Single Nitrogen-Vacancy Centres in Diamond. *New J. Phys.* **13.** doi:10.1088/1367-2630/13/2/025013 (2011).

22. Gupta, A., Hacquebard, L. & Childress, L. Efficient Signal Processing for Time-Resolved Fluorescence Detection of Nitrogen-Vacancy Spins in Diamond. *J. Opt. Soc. Am. B, JOSAB* **33.** doi:10.1364/JOSAB.33.000B28 (2016).

23. Tetienne, J.-P., Rondin, L., Spinicelli, P., Chipaux, M., Debuisschert, T., Roch, J.-F. & Jacques, V. Magnetic-Field-Dependent Photodynamics of Single NV Defects in Diamond: An Application to Qualitative All-Optical Magnetic Imaging. *New J. Phys.* **14.** doi:10.1088/1367-2630/14/10/103033 (2012).

24. Fox, M. *Quantum Optics: An Introduction* https://doi.org/10.1093/oso/9780198566724.001.0001 (2024) (Oxford University Press, Incorporated, 2006).

25. Plakhotnik, T. & Aman, H. NV-centers in Nanodiamonds: How Good They Are. *Diamond and Related Materials* **82.** doi:10.1016/j.diamond.2017.12.004 (2018).

26. Inam, F. A. *et al.* Emission and Nonradiative Decay of Nanodiamond NV Centers in a Low Refractive Index Environment. *ACS Nano* **7.** doi:10.1021/nn304202g (2013).

27. Baier, S., Bradley, C. E., Middelburg, T., Dobrovitski, V. V., Taminiau, T. H. & Hanson, R. Orbital and Spin Dynamics of Single Neutrally-Charged Nitrogen-Vacancy Centers in Diamond. *Phys. Rev. Lett.* **125.** doi:10.1103/PhysRevLett.125.193601 (2020).

28. Happacher, J. *et al.* Low-Temperature Photophysics of Single Nitrogen-Vacancy Centers in Diamond. *Phys. Rev. Lett.* **128.** doi:10.1103/PhysRevLett.128.177401 (2022).

29. Ernst, S., Scheidegger, P. J., Diesch, S. & Degen, C. L. Modeling Temperature-Dependent Population Dynamics in the Excited State of the Nitrogen-Vacancy Center in Diamond. *Phys. Rev. B* **108.** doi:10.1103/PhysRevB.108.085203 (2023).

30. Johansson, J. R., Nation, P. D. & Nori, F. QuTiP: An Open-Source Python Framework for the Dynamics of Open Quantum Systems. *Computer Physics Communications* **183.** doi:10.1016/j.cpc.2012.02.021 (2012).

31. QuTip, D. *Lindblad Master Equation Solver — QuTiP 5.0 Documentation* https://qutip.readthedocs.io/en/qutip-5.0.x/guide/dynamics/dynamics-master.html#the-lindblad-master-equation (2024).

32. QuTip, D. *Solving for Steady-State Solutions — QuTiP 5.0 Documentation* 2024. https://qutip.readthedocs.io/en/qutip-5.0.x/guide/guide-steady.html (2024).

33. *L. Walz (Github)* https://github.com/laeoe (2024).

34. Pogorzelski, J., Horsthemke, L., Homrighausen, J., Stiegekötter, D., Gregor, M. & Glösekötter, P. Compact and Fully Integrated LED Quantum Sensor Based on NV Centers in Diamond. *Sensors* **24.** doi:10.3390/s24030743 (3 2024).

35. Deegan, R. D., Bakajin, O., Dupont, T. F., Huber, G., Nagel, S. R. & Witten, T. A. Capillary Flow as the Cause of Ring Stains from Dried Liquid Drops. *Nature* **389.** doi:10.1038/39827 (1997).

36. Virtanen, P. *et al.* SciPy 1.0: Fundamental Algorithms for Scientific Computing in Python. *Nat Methods* **17.** doi:10.1038/s41592-019-0686-2 (2020).

37. *API Reference: Scipy.Signal.Hilbert* version 1.14.1. 2024. https://docs.scipy.org/doc/scipy/reference/generated/scipy.signal.hilbert.html (2024).

38. *Sinara: An Open-Source Hardware Ecosystem for Quantum Physics* https://sinara-hw.github.io/ (2024).

39. *ARTIQ Manual* https://m-labs.hk/artiq/manual/ (2024).

40. *Advanced Real-Time Infrastructure for Quantum Physics (ARTIQ)* M-Labs, 2024. https://github.com/m-labs/artiq (2024).

41. Krackow, N. *Short Time Fourier Transform Pulse Generator for Trapped Ion Quantum Gates* (TU Berlin, QARTIQ). https://m-labs.hk/thesis_nkrackow.pdf.

42. *M-Labs* https://m-labs.hk/ (2024).

43. Conzatti, R. *A New Control System for a Quantum Network Node* (2023). http://ulb-dok.uibk.ac.at/ulbtirolhs/8998185 (2024).

44. *ARTIQ-8 Released - M-Labs Forum* https://forum.m-labs.hk/d/745-artiq-8-released (2024).

45. Zhu, T., Rhensius, J., Herb, K., Damle, V., Puebla-Hellmann, G., Degen, C. L. & Janitz, E. Multicone Diamond Waveguides for Nanoscale Quantum Sensing. *Nano Lett.* **23.** doi:10.1021/acs.nanolett.3c02120 (2023).

46. Jin, Y., Shen, K., Ju, P., Gao, X., Zu, C., Grine, A. J. & Li, T. Quantum Control and Berry Phase of Electron Spins in Rotating Levitated Diamonds in High Vacuum. *Nat Commun* **15.** doi:10.1038/s41467-024-49175-3 (2024).

47. Andrich, P., Alemán, B. J., Lee, J. C., Ohno, K., de las Casas, C. F., Heremans, F. J., Hu, E. L. & Awschalom, D. D. Engineered Micro- and Nanoscale Diamonds as Mobile Probes for High-Resolution Sensing in Fluid. *Nano Lett.* **14.** doi:10.1021/nl501208s (2014).

48. March, J. E. *et al.* Long Spin Coherence and Relaxation Times in Nanodiamonds Milled from Polycrystalline 12C Diamond. *Phys. Rev. Appl.* **20.** doi:10.1103/PhysRevApplied.20.044045 (2023).

49. Delord, T. Spin-Mechanics with Micro-Particle Levitating in a Paul Trap. *Univ. Paris Sci. Lett.* https://theses.hal.science/tel-03217243v2 (2019).

50. Kern, M., Jeske, J., Lau, D. W. M., Greentree, A. D., Jelezko, F. & Twamley, J. Optical Cryocooling of Diamond. *Phys. Rev. B* **95.** doi:10.1103/PhysRevB.95.235306 (2017).